Amyloid Fibril Formation by $A\beta_{16-22}$, a Seven-Residue Fragment of the Alzheimer's β-Amyloid Peptide, and Structural Characterization by Solid State NMR[†]

John J. Balbach[‡], Yoshitaka Ishii[‡], Oleg N. Antzutkin[§], Richard D. Leapman[‖], Nancy W. Rizzo[‖], Fred Dyda[⊥], Jennifer Reed[#], and Robert Tycko[‡*]

[‡]Laboratory of Chemical Physics, National Institute of Diabetes and Digestive and Kidney Diseases, National Institutes of Health, Bethesda, Maryland
[§]Division of Inorganic Chemistry, Luleå University of Technology, Luleå, Sweden
[‖]Division of Bioengineering and Physical Science, Office of Research Services, National Institutes of Health, Bethesda, Maryland
[⊥]Laboratory of Molecular Biology, National Institute of Diabetes and Digestive and Kidney Disease, National Institutes of Health, Bethesda, Maryland
[#]University of California, San Diego, California
[†]Supported by the Swedish Foundation for International Cooperation in Research and Higher Education (fellowship to ONA), the Japan Society for the Promotion of Science (fellowship to YI), and the Whitaker Foundation through the NIH Biomedical Engineering Summer Internship Program (internship to JR). Solid state NMR techniques used in this work were developed under grants to RT from the NIH Intramural AIDS Targeted Antiviral Program.
[*]corresponding author: National Institutes of Health, Building 5, Room 112, Bethesda, MD 20892-0520. phone 301-402-8272. fax 301-496-0825. e-mail tycko@helix.nih.gov

Biochemistry, in press

[1]Abbreviations: NMR, nuclear magnetic resonance; MQ, multiple quantum; 1D, one-dimensional; 2D, two-dimensional; MAS, magic-angle spinning; CTDQFD, constant-time double-quantum-filtered dipolar recoupling; RFDR, radio-frequency-driven recoupling; TPPM, two-pulse phase modulation; REDOR, rotational echo double resonance; Aβ, Alzheimer's β-amyloid peptide; DRAWS, dipolar recoupling with a windowless sequence; FMOC, fluorenylmethoxycarbonyl; HBTU, H-benzotriazol-1-yl-tetramethyluronium hexafluorophosphate; MBHA, methylbenzhydrylamine; HPLC, high-performance liquid chromatography; FID, free induction decay; CSA, chemical shift anisotropy; EM, electron microscopy; FWHM, full width at half maximum; RMS, root-mean-squared.

Abstract

The seven-residue peptide N-acetyl-Lys-Leu-Val-Phe-Phe-Ala-Glu-NH_2, called $A\beta_{16-22}$ and representing residues 16 through 22 of the full-length β-amyloid peptide associated with Alzheimer's disease, is shown by electron microscopy to form highly ordered fibrils upon incubation of aqueous solutions. X-ray powder diffraction and optical birefringence measurements confirm that these are amyloid fibrils. The peptide conformation and supramolecular organization in $A\beta_{16-22}$ fibrils are investigated by solid state ^{13}C NMR measurements. Two-dimensional magic-angle spinning (2D MAS) exchange and constant-time double-quantum-filtered dipolar recoupling (CTDQFD) measurements indicate a β-strand conformation of the peptide backbone at the central phenylalanine. One-dimensional and two-dimensional spectra of selectively and uniformly labeled samples show ^{13}C NMR linewidths less than 2 ppm, demonstrating that the peptide, including amino acid sidechains, has a well ordered conformation in the fibrils. Two-dimensional ^{13}C-^{13}C chemical shift correlation spectroscopy permits a nearly complete assignment of backbone and sidechain ^{13}C NMR signals and indicates that the β-strand conformation extends across the entire hydrophobic segment from Leu17 through Ala21. ^{13}C multiple quantum (MQ) NMR and $^{13}C/^{15}N$ rotational echo double resonance (REDOR) measurements indicate an antiparallel organization of β-sheets in the $A\beta_{16-22}$ fibrils. These results suggest that the degree of structural order at the molecular level in amyloid fibrils can approach that in peptide or protein crystals, suggest how the supramolecular organization of β-sheets in amyloid fibrils can be dependent on the peptide sequence, and illustrate the utility of solid state NMR measurements as probes of the molecular structure of amyloid fibrils. $A\beta_{16-22}$ is among the shortest fibril-forming fragments of full-length β-amyloid reported to date, and hence serves as a useful model system for physical studies of amyloid fibril formation.

The molecular structures of amyloid fibrils, which are formed by a wide variety of peptides and proteins with unrelated sequences and disparate lengths (*1, 2*), are largely unknown because of the intrinsically noncrystalline and insoluble nature of these materials. Until recently, structural information about amyloid fibrils at the molecular level has come primarily from x-ray diffraction measurements on oriented fibril bundles (*2-4*), which yield the characteristic "cross-β" diffraction pattern that is one of the defining features of amyloid fibrils. The diffraction data are generally interpreted as indicating the presence of ribbon-like β-sheet structures, with peptide chains in β-strand conformations running roughly perpendicular to the long axes of the fibrils and hydrogen bonds between peptide chains running roughly parallel to the long axes. The resulting ribbons of β-sheets may be laminated in several layers (*2, 3*), although other interpretations have been proposed (*4, 5*). Negatively-stained electron micrographs of amyloid fibrils show unbranched structures, typically 50 to 150 Å in diameter and more than 1 μm in length, often with an apparent periodic twist (*4, 6-15*). The similarity of the electron micrographs of amyloid fibrils from different sources is remarkable. Recently, atomic force microscopy has been used to obtain images of amyloid fibrils with higher resolution and to examine the mechanism and kinetics of fibril assembly (*16-20*). Recent cryo-electron microscopy studies support the cross-β structure of amyloid fibrils (*21*).

Solid state NMR measurements developed for structural studies of noncrystalline solids are ideally suited for molecular-level structural studies of amyloid fibrils. Two types of structural information are of interest, namely information about the molecular conformations of peptides and proteins in amyloid fibrils and information about the supramolecular organization of the fibrils, *i.e.*, about the intermolecular interactions and packing. Griffin, Lansbury, and coworkers (*22, 23*) used rotational resonance (*22, 24*) and spin echo (*23*) solid state NMR techniques in structural studies of fibrils formed by the nine-residue peptide $A\beta_{34-42}$, which represents the hydrophobic C-terminal portion of the 42-residue form of the Alzheimer's β-amyloid peptide. Their data indicate a β-strand conformation of the peptide and an antiparallel organization of β-sheets. Lynn, Botto, Meredith, and coworkers (*12, 25, 26*) used the DRAWS solid state NMR technique (*27*) to characterize the peptide conformation and the supramolecular organization of fibrils formed by the 26-residue peptide $A\beta_{10-35}$, which represents residues 10 through 35 of the Alzheimer's β-amyloid peptide and includes both hydrophobic and non-hydrophobic segments. Their data support an in-register, *parallel* organization of β-sheets in these fibrils. We have recently introduced solid state multiple quantum (MQ) ^{13}C NMR spectroscopy (*28, 29*) as a structural probe of biopolymers, based on the time-reversible MQ excitation techniques developed originally by Pines and coworkers (*30-34*). MQNMR data on fibrils formed by the full-length, 40-residue Alzheimer's β-amyloid peptide $A\beta_{1-40}$ also indicate an in-register, parallel organization of β-sheets (*35*). These solid state NMR studies provide molecular-level experimental constraints on structural models of amyloid fibrils. In particular, the solid state NMR data on $A\beta_{10-35}$ and $A\beta_{1-40}$ fibrils contradict a common assumption in modeling of β-amyloid fibrils (*5, 9, 36-38*) that these fibrils are necessarily constructed from antiparallel β-sheets. Evidence for antiparallel β-sheets in amyloid fibrils comes primarily from infrared spectra (*6, 11*), which exhibit an amide I band near 1690 cm^{-1} that has been shown to be characteristic of antiparallel β-sheets in model systems (*39*). Intramolecular antiparallel β-sheets, as proposed in structural models for β-amyloid fibrils (*5, 9, 36, 37*) but not yet established experimentally, may account for the infrared results on full-length Aβ fibrils, or other structural explanations may be forthcoming.

In this paper, we report the formation of amyloid fibrils by the seven-residue peptide N-acetyl-Lys-Leu-Val-Phe-Phe-Ala-Glu-NH_2 and describe structural measurements on these fibrils by solid state NMR. The peptide, which we call $A\beta_{16-22}$, comprises residues 16 through 22 of the Alzheimer's β-amyloid peptide with acetyl and amide capping groups at the N- and C-termini. $A\beta_{16-22}$ is among the shortest fibril-forming β-amyloid fragments yet reported (*6-10, 13*). As such, it is an appealing model system for physical studies of fibril formation. This region of the β-amyloid peptide is of particular interest because residues 17 through 21 have been proposed to constitute a hydrophobic core that is essential for fibrillization of full-length β-amyloid peptides (*8, 40-43*). In addition, peptides containing this region have been shown to inhibit fibrillization of full-length β-amyloid peptides, presumably by complexation with monomeric or oligomeric forms of the full-length peptides (*43-46*). As shown below, the low molecular weight of $A\beta_{16-22}$ leads to a high degree of resolution in one-dimensional (1D) and two-dimensional (2D) solid state ^{13}C magic-angle spinning (MAS) NMR spectra of selectively and uniformly labeled $A\beta_{16-22}$ fibril samples. These spectra show unusually narrow lines for a noncrystalline solid, demonstrating that the peptide conformation (including both sidechain and backbone conformations) is well ordered in the fibrillized state. We report quantitative measurements of the peptide backbone conformation, using the 2D MAS exchange (*47-49*) and constant-time double-quantum-filtered dipolar recoupling (*50*) (CTDQFD) techniques, that indicate a β-strand conformation. A β-strand conformation for the entire hydrophobic segment from Leu17 through Ala21 is supported by ^{13}C chemical shifts determined from 2D chemical shift correlation spectra. ^{13}C MQNMR and $^{13}C/^{15}N$ rotational echo double resonance (REDOR) (*51-53*) data indicate an *antiparallel* organization of β-sheets in $A\beta_{16-22}$ fibrils, as in $A\beta_{34-42}$ but not in $A\beta_{10-35}$ or $A\beta_{1-40}$. Comparison of the supramolecular organization in $A\beta_{16-22}$ with that in the other amyloid fibrils investigated by solid state NMR suggests that hydrophobic interactions may be the principal determinant of supramolecular organization and that electrostatic interactions play a secondary role.

Materials and Methods

Peptide synthesis and fibrillization

$A\beta_{16-22}$ samples were synthesized on a Perkin-Elmer/Applied Biosystems Model 433A solid phase peptide synthesizer, using standard FMOC synthesis and cleavage protocols, a Rink amide MBHA resin (Peptides International), and HBTU activation. Samples were synthesized with no isotopic labels, with ^{13}C labels at carbonyl sites of Val18 and Phe19, with a ^{13}C label at the methyl carbon of Ala21, with a ^{13}C label at the carbonyl carbon of Leu17 and a ^{15}N label at the amide nitrogen of either Phe20 or Ala21, and with uniform ^{13}C and ^{15}N labeling in the hydrophobic segment from Leu17 through Ala21. Isotopically labeled FMOC-protected amino acids were obtained from Cambridge Isotopes Laboratories and Isotec. Unprotected ^{13}C-labeled alanine was protected by Midwest Biotech. The doubly ^{13}C-labeled and uniformly $^{13}C,^{15}N$-labeled samples were diluted to 20% and 10%, respectively, by mixing labeled and unlabeled synthesis resins in the appropriate ratios before cleavage. Samples were purified by high-performance liquid chromatography (HPLC), using a water/acetonitrile gradient with 0.1% trifluoroacetic acid and a Vydac C18 reverse-phase column. Final purities were greater than 95%, as determined by electrospray mass spectrometry. After lyophilization of the HPLC fraction containing the peptide, fibrillized samples were prepared by incubation of aqueous $A\beta_{16-}$

$_{22}$ solutions at a peptide concentration of approximately 200 μM, a temperature of 24° C, and with 1.0 mM phosphate buffer at pH 7.0. In the case of the selectively ^{13}C,^{15}N-labeled samples prepared for REDOR measurements, the buffer concentration was 10 mM. In all cases except the doubly ^{13}C-labeled sample, 0.01% NaN_3 was added to inhibit bacterial and fungal growth. After approximately 10 days of incubation, solutions were either evaporated to dryness over a period of several days or centrifuged to permit collection of precipitated material, which was then dried under a $N_{2(g)}$ stream. Sample sizes were 1 to 5 mg in all NMR measurements. We estimate that these samples contain 80-90% fibrils, with the remaining material being unfibrillized peptide, based on the linewidths and lineshapes in the solid state NMR specta (see below). Further evidence for a high degree of fibrillization is provided by the electron microscopy (EM), optical microscopy, and x-ray diffraction results described below. In addition, the Fourier-transform infrared spectrum of one of our fibrillized $A\beta_{16-22}$ samples (the doubly-^{13}C-labeled sample in Fig. 2) was obtained in the form of a KBr pellet. This spectrum shows a strong amide I band at 1634 cm^{-1}, with a width of 25 cm^{-1}, and a weaker band at 1692 cm^{-1}. These amide I bands are characteristic of β-sheets in amyloid fibrils. The 1692 cm^{-1} band is often interpreted as a signature of antiparallel β-sheets (*6, 11, 39*), in agreement with the solid state NMR results described below.

Solid state NMR spectroscopy

NMR measurements were carried out on Varian/Chemagnetics Infinity-400 spectrometers, at ^{13}C NMR frequencies of 100.4 or 100.8 MHz. Varian/Chemagnetics MAS probes were used. All measurements were at room temperature. Rotor-synchronized 2D MAS exchange and CTDQFD measurements on the doubly ^{13}C-labeled $A\beta_{16-22}$ sample were carried out as previously described (*47, 48, 50*) at MAS frequencies of 2.5 kHz and 4.0 kHz, respectively, using a probe with a 6.0 mm rotor diameter. The radio-frequency (rf) pulse sequences are shown in Figs. 3a and 3b. Proton decoupling fields were 85 kHz in amplitude, and TPPM (*54*) was employed in intervals between ^{13}C pulses in the rf-driven recoupling (RFDR) (*55, 56*) periods of CTDQFD measurements. ^{13}C radio-frequency (rf) fields were 50 kHz in amplitude, except that 180° pulses during RFDR periods were 36.5 kHz in amplitude. Total signal averaging times on approximately 3 mg of fibrillized $A\beta_{16-22}$ in which 20% of the molecules were doubly ^{13}C-labeled were 60 hr and 40 hr for 2D MAS exchange and CTDQFD measurements, respectively, using a recycle delay of 0.5 s for 2D MAS exchange and 1.0 s for CTDQFD measurements. The exchange period in the 2D MAS exchange measurements was 500 ms.

MQNMR, REDOR, and 2D chemical shift correlation measurements used a probe with a 3.2 mm rotor diameter. MQNMR measurements were performed without MAS and employed the time-reversible multiple pulse sequence of Suter *et al.* (*33*), modified by the insertion of 180° pulses to average out chemical shifts and resonance offsets and by incorporation into a double-resonance technique with cross-polarization and proton decoupling as previously described (*28, 35*) and shown in Fig. 8. The length of a complete rf pulse cycle, consisting of eight 90° pulses and 24 180° pulses at the ^{13}C frequency, was 4.8 ms. The ^{13}C rf amplitude was approximately 41.7 kHz during the multiple pulse sequence, but pulse lengths were carefully adjusted to maximize the 10-, 11-, and 12-quantum signals from L-methionine-*methyl*-^{13}C powder with τ_{MQ} = 19.2 ms after minimization of rf phase transients with appropriate tune-up sequences on ^{13}C-methanol. Proton decoupling fields were 140 kHz during MQ preparation and mixing, with TPPM phase modulation employed in the intervals between ^{13}C pulses. Total signal averaging

times for MQNMR measurements on approximately 4 mg of fibrillized $A\beta_{16-22}$ were 11 hr, 21 hr, and 43 hr for τ_{MQ} = 4.8 ms, 9.6 ms, and 14.4 ms, respectively, using a recycle delay of 1.0 s. Extensive block averaging was used to minimize artifactual MQ signals that might otherwise arise from spectrometer instabilities during long experiments. Because the pulse sequence of Suter *et al.* creates a single-quantum effective dipole-dipole coupling Hamiltonian and the initial state of the ^{13}C spin system is transverse magnetization, an intense 1-quantum signal is observed at small values of τ_{MQ} and both even- and odd-order MQ signals develop at larger values of τ_{MQ}.

^{13}C-detected $^{13}C/^{15}N$ REDOR measurements were carried out with the pulse sequence reported by Anderson *et al*. (*53*), in which one 180° pulse per rotor period is applied to both ^{13}C and ^{15}N nuclei, at a MAS frequency of 5.0 kHz. ^{13}C and ^{15}N rf amplitudes were 50 kHz and 44 kHz, and the proton decoupling field during the REDOR pulse train was 110 kHz. Total signal acquisition times for REDOR data in Fig. 12 were 64 hr per sample, using a 1.0 s recycle delay and approximately 1 mg of fibrillized $A\beta_{16-22}$.

2D chemical shift correlation experiments were carried out with a phase-sensitive 2D exchange pulse sequence at a MAS frequency of 24.0 kHz. Amplitude-modulated cross-polarization was used to prepare ^{13}C polarization (*57*), with ^{1}H and ^{13}C rf fields mismatched by the MAS frequency. Proton decoupling fields were 110 kHz, with TPPM employed during the t_1 and t_2 periods. Hypercomplex 2D data were collected by varying the phase of the 90° pulse at the end of t_1. An RFDR sequence, with one 12.5 μs ^{13}C 180° pulse per rotation period, was used to recouple ^{13}C-^{13}C dipole-dipole interactions during the exchange period, which was set to 2.6 ms in order to produce strong crosspeaks only between directly-bonded ^{13}C nuclei. The 2D spectrum in Fig. 7 was acquired in 39 hr on approximately 4 mg of fibrillized $A\beta_{16-22}$ in which 10% of the molecules were isotopically labeled, with 123 t_1 points, a t_1 increment of 40 μs, a 2.2 s recycle delay, and 256 scans per free-induction decay (FID).

Numerical simulations of NMR measurements

Experimental 2D MAS exchange, CTDQFD, REDOR, and MQNMR data were analyzed by comparison with numerical simulations using FORTRAN programs written specifically for this purpose. 2D MAS exchange and CTDQFD data were simulated over a grid of ϕ and ψ values, representing the peptide backbone conformation between the two ^{13}C-labeled carbonyl sites, in 5° increments as previously described (*47*, *48*, *50*). These simulations assumed planar peptide bonds, standard chemical bond lengths and angles, and a standard carbonyl ^{13}C chemical shift anisotropy (CSA) tensor orientation with the δ_{33} axis perpendicular to the carbonyl plane and the δ_{11} axis at an angle of 40° to the C-N bond (*47*, *48*, *50*, *58-61*). Uncertainty in ϕ and ψ values derived from the comparison of experimental and simulated data due to uncertainty in the assumed CSA tensor orientation is estimated to be ±5°. Additional uncertainty in the ϕ and ψ values arising from finite signal-to-noise in the experimental data appears explicitly in the χ^2 contour plots described below. Average CSA principal values for the two ^{13}C-labeled carbonyl sites in $A\beta_{16-22}$ fibrils were determined from MAS sideband analysis (*62*) as described below. 2D MAS exchange crosspeak amplitudes were calculated and analyzed for sidebands of order -2 to +2. Because the labeled Val18 and Phe19 carbonyl sites did not give fully resolved NMR lines, intrasite crosspeaks resulting from spin-lattice relaxation of directly bonded amide ^{14}N nuclei were not resolved from intersite crosspeaks and were therefore included in the analysis (*47*, *48*).

For analysis of MQNMR data, MQ signal amplitudes were calculated at values of τ_{MQ} employed in the experiments for the models of β-sheet organization described below, using a

nine-spin system represented by a 512 X 512 density matrix and a time-independent effective dipole-dipole interaction Hamiltonian of the form ideally created by the time-reversible MQ excitation sequence of Suter *et al*. (*33*). The accuracy of this idealized treatment of the MQNMR pulse sequence was verified by comparison with simulations that included the time-dependent rf field interaction explicitly. Of the nine ^{13}C spins in the MQNMR simulations, seven represented ^{13}C labels at positions dictated by the structural model and two represented natural-abundance ^{13}C at random positions. MQ signal amplitudes were averaged over the random positions of the natural-abundance spins and over the external field direction relative to the labels.

REDOR data were simulated assuming an ideal REDOR pulse sequence that produces an effective Hamiltonian containing only heteronuclear dipole-dipole coupling terms, and assuming that the single carbonyl ^{13}C label in each peptide chain is coupled only to the amide ^{15}N labels in the two neighboring peptide chains within a single β-sheet. The accuracy of idealized REDOR simulations was confirmed by comparison with simulations that included finite rf pulse widths as well as ^{13}C and ^{15}N CSA. Simulated REDOR curves were found to be insensitive to variations in rf amplitudes by up to 10% of the nominal amplitude.

Electron microscopy

Carbon film substrates for EM were prepared by evaporation from a carbon rod source onto freshly cleaved mica in an Edwards Auto 306 coating system. Films were floated off in deionized water and picked up on lacy Formvar/carbon films (EM Sciences) supported on 200 mesh copper grids. Grids were glow-discharged in air prior to peptide deposition. 5 μl aliquots of an incubated $A\beta_{16\text{-}22}$ solution were applied to EM grids and allowed to adsorb for two minutes. Grids were then washed ten times in deionized water before staining by passing through two drops of 1% uranyl acetate. Excess fluid was blotted off and grids were allowed to dry in air. Transmission electron micrographs were recorded using a Philips/FEI CM120 electron microscope and Gatan GIF100 imaging filter equipped with a cooled slow scan CCD camera. Images were acquired and processed by means of the Digital Micrograph program (Gatan).

X-ray diffraction

A portion of one of the $A\beta_{16\text{-}22}$ samples prepared for REDOR measurements was packed into a 0.7 mm quartz capillary. Diffraction data were collected using Ni-filtered and double-mirror focussed Cu Kα radiation (1.54 Å wavelength) generated in a rotating anode source operated at 50 kV and 100 mA. The sample was oscillated over an angle of 90° and exposed for 30 min. Diffraction data were recorded on a Rigaku Raxis IIC imaging plate detector and processed with an image display program supplied by Molecular Structure Corp.

Results

Electron microscopy, x-ray diffraction, and optical birefringence indicate amyloid fibril formation

Figure 1a shows negatively-stained electron micrographs of $A\beta_{16\text{-}22}$ fibrils deposited from a 200 μM aqueous solution of the peptide after incubation for 15 days at 24° C and pH 6.8. Fibrils with lengths ranging from 300 Å to over 8000 Å and apparent diameters ranging from 100 Å to 240 Å are observed. These fibrils appear to be bundles of thinner filaments, with diameters of 50 Å or less. In a fully extended β-strand conformation, a single $A\beta_{16\text{-}22}$ molecule

would be approximately 25 Å in length. No nonfibrillar aggregates of $A\beta_{16-22}$ are observed in the electron micrographs.

A portion of a centrifuged pellet from an incubated $A\beta_{16-22}$ solution was spread on a microscope slide, stained with 10 μl of alkaline Congo Red solution (Sigma), rinsed with ethanol, and covered with a cover slip. The deposited $A\beta_{16-22}$ material appeared pink in bright field optical microscope images and exhibited the pronounced green birefringence characteristic of amyloid films (*63*) when viewed between crossed polarizers (data not shown). The same centrifuged pellet was subsequently dried under a $N_{2(g)}$ stream for REDOR NMR and x-ray diffraction measurements.

Figure 1b shows results of x-ray diffraction measurements on the dried powder. Peaks in intensity at scattering angles (2θ) of 8.9° and 18.8° are observed, corresponding to the 9.9 Å and 4.7 Å periodicities observed in fiber diffraction measurements on amyloid fibrils from a variety of sources (*2-4*). The 4.7 Å periodicity is commonly attributed to the spacing between peptide chains within a β-sheet, while the 9.9 Å periodicity is attributed to the spacing between β-sheet layers.

Because the true periodicity of peptide chains within an antiparallel β-sheet is approximately 2 X 4.7 Å = 9.4 Å, one might expect a peak in Fig. 1b at $2\theta \approx 9.4°$ for consistency with the solid state NMR results described below. Although such a peak has been reported in the meridional x-ray scattering from oriented $A\beta_{1-28}$ fibrils (*8*), this peak is not generally reported (*4, 7, 11*) and has been argued to be systematically absent by symmetry from diffraction patterns of amyloid fibrils composed of antiparallel β-sheets (*64*).

One-dimensional ^{13}C NMR indicates structural order

Figure 2 shows ^{13}C MAS NMR spectra of a fibrillized $A\beta_{16-22}$ sample in which 20% of the peptide molecules are ^{13}C-labeled at the carbonyl carbons of both Val18 and Phe19, obtained at MAS frequencies of 6.0 kHz (Fig. 2a) and 2.0 kHz (Fig. 2b). The carbonyl signal centered at 171 ppm has a full-width-at-half-maximum (FWHM) of 1.7 ppm, but this linewidth results from the overlap of somewhat narrower lines from the two different labeled sites (inset to Fig. 2a). The carbonyl lineshape exhibits a tail on the downfield edge that we attribute to a small fraction (roughly 15%) of unfibrillized peptides. Isotropic chemical shifts of carbonyl carbons are known to be sensitive to secondary structure, with carbonyl carbons in β-strands being shifted approximately 1-3 ppm upfield from the random coil value (*65*). The observed chemical shifts and the fact that the tail is on the downfield edge are consistent with the β-strand conformation in the fibrils demonstrated below. The spectrum in Fig. 2b shows the spinning sideband pattern characteristic of rigid carbonyl ^{13}C sites. From analysis of the spinning sideband intensities (*62*), we determine the average chemical shift anisotropy (CSA) principal values for Val18 and Phe19 to be $(\delta_{11}, \delta_{22}, \delta_{33}) = (240 \text{ ppm}, 178 \text{ ppm}, 94 \text{ ppm})$. CSA principal values could not be determined for the two labeled sites separately because their signals were not fully resolved.

From fitting the observed carbonyl lineshape to the sum of two Gaussian lines, we estimate the individual carbonyl linewidths to be 1.0 ppm and the chemical shift difference to be 0.9 ppm. The aliphatic region of the ^{13}C MAS spectrum (15 to 60 ppm) shows natural-abundance lines with FWHM of 1.0 ppm. These linewidths are comparable to linewidths observed under similar conditions in ^{13}C MAS NMR spectra of polycrystalline peptides (*47, 50*) and are narrower than those observed in frozen solutions of peptides with well ordered helical conformations (*50, 66*) or in a tightly bound peptide/antibody complex (*67*).

$A\beta_{16-22}$ adopts a β-strand conformation in the fibrils

The peptide backbone conformation in $A\beta_{16-22}$ fibrils was investigated by 2D MAS exchange (*47-49*) and CTDQFD (*50*) measurements on the same sample used in Fig. 2. The rf pulse sequences for these measurements are shown in Figs. 3a and 3b. These two solid state NMR techniques, which have been applied previously in a variety of structural studies (*47, 48, 50, 66, 67*), provide constraints on the dihedral angles ϕ and ψ that define the backbone conformation between the two labeled carbonyl sites, in this case the ϕ and ψ angles of Phe19, the central residue in $A\beta_{16-22}$. 2D MAS exchange spectra, obtained in the limit of full exchange, are sensitive to the relative orientations of the CSA tensors of the two labeled carbonyls but not the internuclear distance. CTDQFD measurements are primarily sensitive to the internuclear distance, with a weaker dependence on the relative CSA orientations arising from the dependence of ^{13}C-^{13}C dipolar recoupling on the CSA tensors when the RFDR recoupling sequence is employed (*50, 55, 56, 68*). The 2D MAS exchange spectrum of the fibrillized, doubly-labeled $A\beta_{16-22}$ sample is shown in Fig. 4. Crosspeaks that connect the carbonyl spinning sideband lines are evident. The intensities of these crosspeaks, which contain the structural information, were measured by integration over rectangular areas centered on the expected crosspeak positions. Intensities of crosspeaks symmetrically disposed about the diagonal of the 2D spectrum were added together before comparison with simulations. The root-mean-squared (RMS) noise σ_{2D} was measured by integration over rectangular areas centered on regions of the 2D MAS exchange spectrum that contain no signals. CTDQFD data are shown in Fig. 5a. The dependence of the double-quantum-filtered carbonyl signal on the effective dipolar evolution time $\tau_D = (M - N)\tau_R$, where τ_R is the MAS rotation period, was measured by integrating the spectra over 10-ppm-wide intervals centered on the isotropic carbonyl chemical shift and on the two spinning sidebands visible in Fig. 5a. The rms noise σ_{DQ} was measured by integrating the spectra over intervals that contain no signals. The dependence of the experimental CTDQFD signal amplitude on τ_D is plotted in Fig. 5b, along with simulations for several ϕ,ψ pairs.

Figure 6 shows contour plots of the χ^2 deviation between experimental data and simulations for the 2D MAS exchange measurements ($\chi_{2D}{}^2$, Fig. 6a), the CTDQFD measurements ($\chi_{DQ}{}^2$, Fig. 6b), and the combined measurements ($\chi_{SUM}{}^2$, Fig. 6c), using the definitions

$$\chi_{2D}(\phi,\psi)^2 \equiv \frac{1}{\sigma_{2D}{}^2}\sum_{m=1}^{N_{2D}}[E_{2D}(m) - C_{INTER}(\phi,\psi)S_{INTER}(m;\phi,\psi) - C_{INTRA}(\phi,\psi)S_{INTRA}(m)]^2 \qquad (1a)$$

$$\chi_{DQ}(\phi,\psi)^2 \equiv \frac{1}{\sigma_{DQ}{}^2}\sum_{m=1}^{N_{DQ}}[E_{DQ}(m) - D(\phi,\psi)S_{DQ}(m;\phi,\psi)]^2 \qquad (1b)$$

$$\chi_{SUM}(\phi,\psi)^2 \equiv \chi_{2D}(\phi,\psi)^2 + \chi_{DQ}(\phi,\psi)^2 \qquad (1c)$$

In Eqs. (1a) and (1b), N_{2D} and N_{DQ} are the numbers of experimental data points, with the values 10 (after symmetrization of the 2D MAS exchange spectrum) and 6, respectively. $E_{2D}(m)$ and $E_{DQ}(m)$ are the experimental data. $S_{INTER}(m;\phi,\psi)$ and $S_{DQ}(m;\phi,\psi)$ are the calculated intersite crosspeak intensity in the 2D MAS exchange spectrum, resulting from exchange of nuclear spin polarization between the two labeled carbonyl sites during the period τ_e in Fig. 3a, and the calculated CTDQFD signal intensity for the ϕ,ψ values assumed in the calculations. $S_{INTRA}(m)$ is

the calculated contribution of intrasite exchange to the crosspeak intensity, which results from spin-lattice relaxation of amide ^{14}N nuclei during τ_e (*47, 48*). $S_{INTRA}(m)$ is independent of the peptide conformation. The scaling coefficients $C_{INTER}(\phi,\psi)$, $C_{INTRA}(\phi,\psi)$, and $D(\phi,\psi)$ are required because the NMR signals are not measured on an absolute scale and because the extent of ^{14}N spin-lattice relaxation is not known. These coefficients are calculated to minimize χ_{2D}^2 and χ_{DQ}^2 for each ϕ,ψ pair.

The absolute minimum in χ_{2D}^2 (Fig. 6a) occurs at ϕ,ψ = -125°,125°. The next lowest local minimum occurs at ϕ,ψ = -50°,-110°. A single strip of minimum χ_{DQ}^2 is observed (Fig. 6b). When the two data sets are combined, a single deep minimum in χ_{SUM}^2 (Fig. 6c) occurs at ϕ,ψ = -130°,115°. The value of χ_{SUM}^2 at this minimum is 10.2, which is less than $N_{2D} + N_{DQ} - 3$ (*i.e.*, number of data points minus number of adjustable parameters), indicating a good fit to the experimental data. These ϕ and ψ values indicate an extended backbone conformation, *i.e.*, a β-strand conformation, at Phe19 in fibrillized $A\beta_{16\text{-}22}$.

2D MAS exchange and CTDQFD measurements can not distinguish ϕ,ψ from $-\phi,-\psi$, due to symmetries of the nuclear spin interactions (*48*). The possibility that ϕ,ψ = 130°,-115° is ruled out as being energetically unfavorable for a phenylalanine residue.

2D NMR spectroscopy of uniformly labeled $A\beta_{16\text{-}22}$ indicates a high degree of structural order in the fibrils

A fibrillized $A\beta_{16\text{-}22}$ sample was prepared in which all carbon and nitrogen sites in the hydrophobic segment from Leu17 through Ala21 are labeled with ^{13}C or ^{15}N. Labeled molecules were diluted to 10% in unlabeled molecules to reduce effects of intermolecular couplings. A 2D ^{13}C-^{13}C chemical shift correlation spectrum of this sample (Fig. 7) was recorded under fast MAS to explore the feasibility of solid state NMR measurements on uniformly labeled amyloid fibrils, investigate linewidths at backbone and sidechain carbon sites, and measure conformation-dependent ^{13}C chemical shifts. Strong crosspeaks between directly-bonded ^{13}C sites are visible in Fig. 7 that permit chemical shift assignment of the majority of sites. The assignments are summarized in Table 1 and compared with random coil chemical shifts (*69*). The systematic upfield shifts of C_α and carbonyl resonances and systematic downfield shifts of C_β resonances, relative to the random coil chemical shifts, indicate a β-sheet conformation along the entire hydrophobic segment (*65, 70*). ^{13}C linewidths (FWHM) of individual sites estimated from resolved crosspeak lineshapes are all approximately 2 ppm or less. These linewidths include an estimated 0.7 ppm contribution from unresolved ^{13}C-^{13}C scalar couplings, so that the inhomogeneous broadening due to structural disorder is apparently less than 2 ppm, in agreement with the spectra of doubly-labeled $A\beta_{16\text{-}22}$ fibrils in Fig. 2. These linewidths are comparable to ^{13}C linewidths reported for uniformly labeled polycrystalline peptides and proteins (*71-77*). It is well known that ^{13}C linewidths in MAS experiments are sensitive to structural disorder, with backbone and sidechain linewidths from unstructured peptides generally exceeding 4 ppm. Thus, it appears that the molecular conformation, including sidechain conformations, is well ordered in $A\beta_{16\text{-}22}$ fibrils. The degree of local structural order approaches that of a peptide or protein crystal, although the long-range translational symmetry of a crystal is lacking.

Multiple quantum NMR and REDOR measurements indicate an antiparallel organization of β-sheets in $A\beta_{16\text{-}22}$ fibrils

The supramolecular organization of $A\beta_{16\text{-}22}$ fibrils was investigated initially by ^{13}C MQNMR measurements (*28, 29, 35*). These measurements contain structural information because observation of an m-quantum ^{13}C NMR signal requires that at least m ^{13}C nuclei be coupled by magnetic dipole-dipole interactions (*31-33, 78*). The strength of these interactions is specified by the dipole-dipole coupling constant $d_{CC} \equiv \frac{\gamma^2 \hbar}{2\pi R^3}$, where γ is the nuclear magnetogyric ratio and R is the internuclear distance. When $R \approx 4.8$ Å, the typical distance between hydrogen-bonded peptide chains in a β-sheet, $d_{CC} \approx 70$ Hz for ^{13}C pairs. The time scale for excitation of MQ coherences is roughly $1/d_{CC}$. Thus, the amplitudes of MQ signals in MQNMR spectra of ^{13}C-labeled $A\beta_{16\text{-}22}$ fibrils can be used to probe the organization of β-sheets when the MQ excitation period τ_{MQ} is of order 15 ms.

Experimental MQNMR spectra of a fibrillized $A\beta_{16\text{-}22}$ sample in which all peptide molecules were labeled with ^{13}C at the methyl carbon of Ala21, obtained with the rf pulse sequence in Fig. 8, are shown in Fig. 9 for τ_{MQ} values of 4.8 ms, 9.6 ms, and 14.4 ms. The labeling scheme in these measurements follows the idea of using solid state NMR measurements on singly ^{13}C-labeled peptides to probe β-sheet organization originally introduced by Lynn, Botto, Meredith, and coworkers (*12, 25, 26*). In an in-register, parallel β-sheet (Fig. 10a), the ^{13}C labels would form a nearly linear chain with approximately 4.8 Å internuclear distances. In an antiparallel β-sheet (Fig. 10b), the labels would form a nearly planar zig-zag pattern, with significantly larger internuclear distances, weaker dipole-dipole couplings, and hence weaker MQNMR signals. The experimental spectra show increasing amplitudes of two-quantum and three-quantum signals relative to the one-quantum signal with increasing τ_{MQ}. No four-quantum or higher-order signals are observed above the noise, even at $\tau_{MQ} = 14.4$ ms. These spectra differ significantly from MQNMR spectra of singly-labeled $A\beta_{1\text{-}40}$ and $A\beta_{10\text{-}35}$ fibrils (data not shown), which were obtained under identical conditions and clearly showed four-quantum signals as well as greater three-quantum amplitudes (*35*). MQNMR spectra of $A\beta_{1\text{-}40}$ and $A\beta_{10\text{-}35}$ fibrils are in good agreement with simulations based on an in-register, parallel β-sheet model (*35*). The spectra in Fig. 9 indicate that the organization of β-sheets in $A\beta_{16\text{-}22}$ fibrils is qualitatively different from that in $A\beta_{1\text{-}40}$ and $A\beta_{10\text{-}35}$ fibrils.

The MQNMR spectra in Fig. 9 were analyzed quantitatively by comparison of the experimental MQ signal amplitudes with numerical simulations for in-register parallel and antiparallel β-sheet models. Simulations were carried out on nine-spin systems, as previously described (*35*). Seven spins, representing methyl ^{13}C labels on Ala21, were placed at positions dictated by the structural models in Fig. 10. For the parallel model, the (x,y,z) coordinates of the seven labels (Å) were (0,4.8i,0), $1 \le i \le 7$. For the antiparallel model, the coordinates were (6.8k,4.8i,0), with $k = (-1)^i$ and $1 \le i \le 7$. The remaining two spins, representing natural-abundance ^{13}C nuclei at other aliphatic carbon sites, were positioned randomly in a rectangular box with a 1.0×10^4 Å^3 volume enclosing the labels. The 7:2 ratio of ^{13}C labels to natural-abundance ^{13}C in the simulations closely approximates the 1.00:0.28 ratio of ^{13}C labels to natural-abundance aliphatic carbons in the actual samples, calculated from the known chemical formula and the expected 1.1% level of natural-abundance ^{13}C. Simulated MQ amplitudes were averaged over the random positions of the natural-abundance spins and over orientation relative to the external magnetic field direction. An overall scaling factor ζ was applied to the simulated

amplitudes $S(n;\tau_{MQ})$ for each model and each value of τ_{MQ} to minimize the squared deviation s^2 between $S(n;\tau_{MQ})$ and the experimental amplitudes $E(n;\tau_{MQ})$, as defined by $s^2 = \sum_{n=2}^{5}[E(n;\tau_{MQ}) - \zeta S(n;\tau_{MQ})]^2$. Zero- and one-quantum signals were not included in s^2 because the experimental zero-quantum amplitudes are especially sensitive to rf inhomogeneity and other pulse imperfections and the one-quantum amplitudes have a significant contribution from natural-abundance ^{13}C nuclei that can only be included in the simulations at an approximate level.

Figure 11 shows that simulations based on the in-register, parallel β-sheet model substantially overestimate the three- and four-quantum signal amplitudes and underestimate the one-quantum signal amplitude. Simulations based on the antiparallel β-sheet model are in better agreement with the experimental MQ amplitudes at all values of τ_{MQ} (note the logarithmic scale in Fig. 11). The agreement between experiments and antiparallel simulations is not truly quantitative, however. In an in-register, antiparallel β-sheet (Fig. 10b), the shortest distance between ^{13}C labels at Ala21 in a single sheet would be greater than 9 Å and may be comparable to (or greater than) distances between labels in different β-sheet layers. Couplings between labels in different layers, which can not be included in the MQ simulations without a detailed model of the interlayer structure, may then affect the MQ signal amplitudes. Couplings to natural-abundance ^{13}C nuclei, which can only be simulated approximately as described above, may also affect the MQ signal amplitudes significantly when the couplings among labels are weak. Thus, highly quantitative agreement between experiments and antiparallel simulations is not expected, even when the true β-sheet organization is antiparallel. The MQNMR data demonstrate that β-sheets in $A\beta_{16-22}$ fibrils do not have an in-register, parallel organization and are consistent with (but do not prove) an antiparallel organization.

Motivated by the MQNMR data, REDOR experiments (*51-53*) were designed to confirm an antiparallel organization and to investigate the hydrogen bonding pattern in the antiparallel β-sheets. Two selectively ^{13}C, ^{15}N-labeled $A\beta_{16-22}$ samples were prepared, one with a ^{13}C label at the carbonyl position of Leu17 and a ^{15}N label at the amide nitrogen of Ala21 (LA sample), the other with a ^{13}C label at the carbonyl position of Leu17 and a ^{15}N label at the amide nitrogen of Phe20 (LF sample). In an antiparallel β-sheet with hydrogen bonding between a ^{13}C-labeled carbonyl and a ^{15}N-labeled amide nitrogen, one expects heteronuclear dipole-dipole couplings $d_{CN} \approx 41$ Hz, corresponding to a 4.2 Å ^{13}C-^{15}N distance. In a parallel β-sheet, the shortest ^{13}C-^{15}N distance is expected to exceed 8 Å, making $d_{CN} < 6$ Hz. Heteronuclear dipole-dipole couplings can be measured in MAS experiments using the REDOR technique developed by Gullion and Schaefer (*51-53*). In these experiments, one measures ^{13}C NMR signals after a dephasing period of length τ_{REDOR} during which a train of rotor-synchronized 180° pulses is applied at the ^{13}C NMR frequency alone (S_0) or at both the ^{13}C and ^{15}N NMR frequencies (S_1). A significant difference signal $\Delta S = S_0 - S_1$ is expected when $\tau_{REDOR} \sim 1/d_{CN}$, *i.e.* $\tau_{REDOR} \sim 25$ ms for a 4.2 Å ^{13}C-^{15}N distance. The dependence of $\Delta S/S_0$ on τ_{REDOR} can be compared with numerical simulations to extract quantitative structural constraints.

Figure 12a shows the results of ^{13}C-detected REDOR measurements on the two fibrillized, selectively ^{13}C,^{15}N-labeled $A\beta_{16-22}$ samples. In both samples, significant values of $\Delta S/S_0$ are observed, providing strong support for an antiparallel β-sheet organization. The growth of $\Delta S/S_0$ with increasing τ_{REDOR} is more rapid in the LA sample than in the LF sample. This observation implies shorter ^{13}C-^{15}N distances in the LA sample than in the LF sample and

provides qualitative support for an in-register, antiparallel structure in which Leu17 is hydrogen-bonded to Ala21, rather than to Phe20 (Fig. 10b).

The REDOR data were analyzed quantitatively by comparison with simulations for a three-spin system, consisting of a single carbonyl ^{13}C label and the two amide ^{15}N labels on neighboring peptide chains. The simulations presented in Fig. 12a assume an in-register, antiparallel β-sheet organization. As depicted in Fig. 12b, the geometry of the antiparallel β-sheet is described by five parameters, namely the hydrogen-bonded ^{13}C-^{15}N distance d_1 connecting Leu17 and Ala21, the interchain ^{15}N-^{15}N distance d_2, the intrachain distance d_3 connecting nitrogen sites of Ala21 and Phe20, the angle θ_1 between d_1 and d_2, and the angle θ_2 between d_1 and d_3. All nuclei are assumed to lie in a single plane. REDOR curves were calculated numerically for both the LA and the LF samples and were scaled in amplitude to minimize χ^2, defined in analogy to Eqs. (1). Fig. 12a shows the results of two such simulations, one assuming an idealized β-sheet geometry (d_1 = 4.2 Å, d_2 = 9.4 Å, d_3 = 3.4 Å, $\theta_1 = 0°$, $\theta_2 = 90°$, χ^2 = 99.9), the other assuming a geometry that is slightly distorted from the idealized case and gives better agreement with the experimental data (d_1 = 4.4 Å, d_2 = 10.0 Å, d_3 = 3.4 Å, $\theta_1 = 10°$, $\theta_2 = 78°$, χ^2 = 61.2). These two simulations demonstrate the sensitivity of REDOR curves to relatively small changes in geometry. The agreement between these simulations and the experimental data is satisfactory given the uncertainties in the precise geometry of the β-sheets and uncertainties regarding the effects of longer-range ^{13}C-^{15}N couplings, small-amplitude molecular motions (which tend to reduce the dipole-dipole coupling strengths and would lead to longer apparent internuclear distances) and rf pulse imperfections on the data. Analogous simulations assuming out-of-register, antiparallel β-sheet structures, with hydrogen bonding of Leu17 to either Phe20 or Glu22, gave significantly poorer fits to the data. We interpret the results as support for an in-register, antiparallel organization of β-sheets in $A\beta_{16-22}$ fibrils.

Discussion

A number of fragments of the Alzheimer's β-amyloid peptide have been shown by other groups to form amyloid fibrils, including $A\beta_{1-28}$, $A\beta_{12-28}$, $A\beta_{14-28}$ (*79*) $A\beta_{1-X}$ with X = 18, 30, 33, and 36 *(7, 8, 13)*, $A\beta_{18-28}$ (*7, 8*), $A\beta_{11-25}$ (*7*), $A\beta_{26-33}$ *(10)*, $A\beta_{34-42}$ (*10, 22*), $A\beta_{10-35}$ (*12, 25, 26*), $A\beta_{10-23}$, $A\beta_{29-42}$, $A\beta_{X-43}$ with X = 4, 8, 10, and 12 (*6*), and $A\beta_{7+X,30-X}$, with $0 \le X \le 7$ (*9*). The results above showing that $A\beta_{16-22}$ also forms amyloid fibrils are especially interesting because $A\beta_{16-22}$ is among the shortest fibrillizing fragments yet reported. As such, $A\beta_{16-22}$ serves as a particularly useful model system for investigations of amyloid fibril structure and the physical basis for amyloid fibril formation. One consequence of the low molecular weight of $A\beta_{16-22}$ is the simplicity of the 1D and 2D solid state NMR spectra, which facilitates the quantitative determination of the ϕ and ψ backbone dihedral angles at Phe19 in the doubly ^{13}C-labeled sample (Figs. 4, 5, and 6) and permits the resolution and assignment of backbone and sidechain ^{13}C NMR lines in the 2D chemical shift correlation spectrum of the uniformly labeled sample (Fig. 7 and Table 1). The ϕ and ψ angles at Phe19, the central residue in $A\beta_{16-22}$, are those of a β-strand. The assigned carbonyl, C_α, and C_β chemical shifts in the uniformly labeled sample deviate systematically from random coil values in a manner indicative of a β-strand conformation throughout the hydrophobic segment from Leu17 through Ala21. These NMR results represent the first application of the 2D MAS exchange and CTDQFD techniques to the determination of the local secondary structure in a specifically labeled peptide fibril and the first

assignment of ^{13}C NMR lines from 2D spectroscopy of a uniformly labeled peptide fibril. The feasibility and utility of these measurements is established by the results reported above. The same techniques can be applied to full-length Alzheimer's β-amyloid fibrils, or amyloid fibrils formed by other peptides and proteins. It will be of particular interest to search for non-β-strand ϕ and ψ values (*i.e.*, turns and helical regions) in higher-molecular-weight peptide fibrils, as observed in β-amyloid peptides in solution (*80-82*) and invoked in structural models for full-length β-amyloid fibrils (*5, 9, 36, 37*), and to carry out multidimensional NMR measurements on full-length β-amyloid fibrils that are uniformly labeled in five-to-ten-residue segments.

A prevalent structural model for β-amyloid fibrils, supported by the "cross-β" pattern observed in x-ray fiber diffraction measurements, describes these fibrils as being constructed from laminated layers of β-sheet, with peptide chains running approximately perpendicular to the long axis of the fibril and hydrogen bonds between peptide chains in each layer running approximately parallel to this axis (*2, 3*). The NMR data indicating a β-strand conformation for the $A\beta_{16-22}$ peptide backbone (Fig. 6 and Table 1) and the x-ray diffraction data indicating the 4.7 Å periodicity of an extended β-sheet (Fig. 1b) suggest that this structural model may apply to $A\beta_{16-22}$ fibrils. Thus, it appears that the β-sheets in an amyloid fibril may be as narrow as 25 Å, corresponding to the approximate end-to-end distance of an $A\beta_{16-22}$ molecule in a β-strand conformation.

Alternative models for β-amyloid fibrils have been proposed, including β-helical models (*5*) and a double-walled tubular model (*4*). It is unclear how a β-helix or double-walled tube could be constructed from a seven-residue peptide in a β-strand conformation, although these models may correctly describe amyloid fibrils constructed from longer peptides.

As stressed above, the ^{13}C NMR lines observed in 1D and 2D spectra of selectively and uniformly labeled $A\beta_{16-22}$ fibrils are remarkably narrow for a noncrystalline solid. The linewidths indicate a high-degree of conformational order. In addition, the 2D MAS exchange and CTDQFD data are well fit by simulations that assume single ϕ and ψ values (Fig. 6), without inclusion of any disordered component in the NMR data and without invocation of a distribution of ϕ and ψ values. These results are strong evidence for a well-defined molecular conformation, including sidechain as well as backbone conformations, in the fibrils. In the absence of such solid state NMR data, it would be unclear whether amyloid fibrils have short-range translational order at the atomic level or merely the approximate periodicity of the peptide chains in β-sheets demanded by x-ray fiber diffraction data. It may also be unclear whether a macroscopic amyloid fibril sample, for which EM images clearly indicate a distribution of fibril morphologies, possesses homogeneous microstructure. The experimental results support a level of local translational order and homogeneity comparable to that in peptide and protein crystals. The precise length scale of translational order remains to be determined, but is likely to exceed tens of angstroms.

The MQNMR and REDOR data rule out an in-register, parallel β-sheet organization for $A\beta_{16-22}$ fibrils and support an antiparallel organization. An in-register, parallel β-sheet organization has been established for $A\beta_{1-40}$ by MQNMR (*35*) and for $A\beta_{10-35}$ fibrils by DRAWS measurements (*12, 25, 26*). An antiparallel β-sheet organization has been established for $A\beta_{34-42}$ fibrils by rotational resonance NMR measurements (*22*). Thus, it appears that amyloid fibrils exhibit a variety of β-sheet organizations, depending on the peptide sequence. A common feature of the $A\beta_{1-40}$ and $A\beta_{10-35}$ sequences is the presence of hydrophobic segments (residues 17 through 22 and 29 through 40 in $A\beta_{1-40}$) that are not symmetrically disposed about the midpoint

of the peptide. In such cases, an in-register, parallel β-sheet organization juxtaposes the hydrophobic segments of neighboring molecules within a β-sheet, producing extended hydrophobic patches, while an antiparallel β-sheet organization necessarily intermingles hydrophobic and non-hydrophobic residues. Hydrophobic interactions may then favor an in-register, parallel organization over an antiparallel organization. The importance of hydrophobic interactions in amyloid fibril formation has been discussed by others (*6, 7, 10, 13*). In contrast, both $A\beta_{16-22}$ and $A\beta_{34-42}$ contain a single central hydrophobic segment, a positive charge at the N-terminus (Lys16 in $A\beta_{16-22}$; the free amino group in $A\beta_{34-42}$), and a negative charge at the C-terminus (Glu22 in $A\beta_{16-22}$; the free carboxylate group in $A\beta_{34-42}$). In other words, $A\beta_{16-22}$ and $A\beta_{34-42}$ are electric dipoles in β-strand conformations. Hydrophobic residues can be juxtaposed in either a parallel or an antiparallel structure. The antiparallel structure may then be favored by electrostatic interactions between the C- and N-termini of neighboring molecules in a β-sheet. Additional measurements on other amyloid fibrils will test the importance of these simple considerations as determinants of supramolecular organization. Sidechain packing and interactions between β-sheet layers may also play important roles in determining the fibril structure.

Taken together, the solid state NMR data on supramolecular organization in full-length Aβ fibrils and Aβ fragment fibrils indicate that the amino acid sequence within a seven-residue segment is insufficient to determine the supramolecular organization uniquely. The sidechains in particular segments of the peptide sequence (*e.g.*, the segments containing residues 16 through 22) must be capable of packing in more than one way, in order to allow both the parallel ($A\beta_{10-35}$ and $A\beta_{1-40}$) and the antiparallel ($A\beta_{16-22}$ and $A\beta_{34-42}$) β-sheet structures observed in different amyloid fibrils containing those segments.

The low molecular weight of $A\beta_{16-22}$ and the quality of the solid state NMR spectra reported above suggest the feasibility of deriving a complete molecular structure of $A\beta_{16-22}$ fibrils from solid state NMR restraints, using additional solid state NMR measurements. With segmental uniform labeling, it may prove possible to determine complete structures of amyloid fibrils formed by longer peptides. Such structures would contribute to the development of a more detailed understanding of the interactions that govern amyloid fibril formation.

Acknowledgments

Numerical simulations of MQNMR experiments were performed on the Silicon Graphics Origin 2000 computer in the NIH Center for Information Technology. We are grateful to Dr. L.K. Pannell for mass spectrometry measurements on peptide samples.

References

1. Sipe, J.D. (1992) *Annu. Rev. Biochem.* **61**, 947-975.
2. Sunde, M., and Blake, C.C.F. (1998) *Q. Rev. Biophys.* **31**, 1-39.
3. Sunde, M., Serpell, L.C., Bartlam, M., Fraser, P.E., Pepys, M.B., and Blake, C.C.F. (1997) *J. Mol. Biol.* **273**, 729-739.
4. Malinchik, S.B., Inouye, H., Szumowski, K.E., and Kirschner, D.A. (1998) *Biophys. J.* **74**, 537-545.
5. Lazo, N.D., and Downing, D.T. (1998) *Biochemistry* **37**, 1731-1735.
6. Hilbich, C., Kisterswoike, B., Reed, J., Masters, C.L., and Beyreuther, K. (1991) *J. Mol. Biol.* **218**, 149-163.
7. Fraser, P.E., McLachlan, D.R., Surewicz, W.K., Mizzen, C.A., Snow, A.D., Nguyen, J.T., and Kirschner, D.A. (1994) *J. Mol. Biol.* **244**, 64-73.
8. Kirschner, D.A., Inouye, H., Duffy, L.K., Sinclair, A., Lind, M., and Selkoe, D.J. (1987) *Proc. Natl. Acad. Sci.* **84**, 6953-6957.
9. Tjernberg, L.O., Callaway, D.J.E., Tjernberg, A., Hahne, S., Lilliehook, C., Terenius, L., Thyberg, J., and Nordstedt, C. (1999) *J. Biol. Chem.* **274**, 12619-12625.
10. Halverson, K., Fraser, P.E., Kirschner, D.A., and Lansbury, P.T. (1990) *Biochemistry* **29**, 2639-2644.
11. Fraser, P.E., Nguyen, J.T., Inouye, H., Surewicz, W.K., Selkoe, D.J., Podlisny, M.B., and Kirschner, D.A. (1992) *Biochemistry* **31**, 10716-10723.
12. Benzinger, T.L.S., Gregory, D.M., Burkoth, T.S., Miller-Auer, H., Lynn, D.G., Botto, R.E., and Meredith, S.C. (2000) *Biochemistry* **39**, 3491-3499.
13. Burdick, D., Soreghan, B., Kwon, M., Kosmoski, J., Knauer, M., Henschen, A., Yates, J., Cotman, C., and Glabe, C. (1992) *J. Biol. Chem.* **267**, 546-554.
14. Jimenez, J.L., Guijarro, J.L., Orlova, E., Zurdo, J., Dobson, C.M., Sunde, M., and Saibil, H.R. (1999) *Embo J.* **18**, 815-821.
15. Serpell, L.C., Sunde, M., Fraser, P.E., Luther, P.K., Morris, E.P., Sangren, O., Lundgren, E., and Blake, C.C.F. (1995) *J. Mol. Biol.* **254**, 113-118.
16. Stine, W.B., Snyder, S.W., Ladror, U.S., Wade, W.S., Miller, M.F., Perun, T.J., Holzman, T.F., and Krafft, G.A. (1996) *J. Protein Chem.* **15**, 193-203.
17. Harper, J.D., Lieber, C.M., and Lansbury, P.T. (1997) *Chem. Biol.* **4**, 951-959.
18. Harper, J.D., Wong, S.S., Lieber, C.M., and Lansbury, P.T. (1999) *Biochemistry* **38**, 8972-8980.
19. Goldsbury, C., Kistler, J., Aebi, U., Arvinte, T., and Cooper, G.J.S. (1999) *J. Mol. Biol.* **285**, 33-39.
20. Tenidis, K., Waldner, M., Bernhagen, J., Fischle, W., Bergmann, M., Weber, M., Merkle, M.L., Voelter, W., Brunner, H., and Kapurniotu, A. (2000) *J. Mol. Biol.* **295**, 1055-1071.
21. Serpell, L.C., and Smith, J.M. (2000) *J. Mol. Biol.* **299**, 225-231.

22. Lansbury, P.T., Costa, P.R., Griffiths, J.M., Simon, E.J., Auger, M., Halverson, K.J., Kocisko, D.A., Hendsch, Z.S., Ashburn, T.T., Spencer, R.G.S., Tidor, B., and Griffin, R.G. (1995) *Nat. Struct. Biol.* **2**, 990-998.
23. Costa, P.R., Kocisko, D.A., Sun, B.Q., Lansbury, P.T., and Griffin, R.G. (1997) *J. Am. Chem. Soc.* **119**, 10487-10493.
24. Raleigh, D.P., Levitt, M.H., and Griffin, R.G. (1988) *Chem. Phys. Lett.* **146**, 71-76.
25. Benzinger, T.L.S., Gregory, D.M., Burkoth, T.S., Miller-Auer, H., Lynn, D.G., Botto, R.E., and Meredith, S.C. (1998) *Proc. Natl. Acad. Sci. U. S. A.* **95**, 13407-13412.
26. Gregory, D.M., Benzinger, T.L.S., Burkoth, T.S., Miller-Auer, H., Lynn, D.G., Meredith, S.C., and Botto, R.E. (1998) *Solid State Nucl. Magn. Reson.* **13**, 149-166.
27. Gregory, D.M., Mitchell, D.J., Stringer, J.A., Kiihne, S., Shiels, J.C., Callahan, J., Mehta, M.A., and Drobny, G.P. (1995) *Chem. Phys. Lett.* **246**, 654-663.
28. Antzutkin, O.N., and Tycko, R. (1999) *J. Chem. Phys.* **110**, 2749-2752.
29. Tycko, R. (1999) *J. Magn. Reson.* **139**, 302-307.
30. Warren, W.S., Weitekamp, D.P., and Pines, A. (1980) *J. Chem. Phys.* **73**, 2084-2099.
31. Yen, Y.-S., and Pines, A. (1983) *J. Chem. Phys.* **78**, 3579-3582.
32. Baum, J., Munowitz, M., Garroway, A.N., and Pines, A. (1985) *J. Chem. Phys.* **83**, 2015-2025.
33. Suter, D., Liu, S.B., Baum, J., and Pines, A. (1987) *Chem. Phys.* **114**, 103-109.
34. Shykind, D.N., Baum, J., Liu, S.B., and Pines, A. (1988) *J. Magn. Reson.* **76**, 149-154.
35. Antzutkin, O.N., Balbach, J.J., Leapman, R.D., Rizzo, N.W., Reed, J., and Tycko, R. (2000) *submitted for publication*.
36. Li, L.P., Darden, T.A., Bartolotti, L., Kominos, D., and Pedersen, L.G. (1999) *Biophys. J.* **76**, 2871-2878.
37. Chaney, M.O., Webster, S.D., Kuo, Y.M., and Roher, A.E. (1998) *Protein Eng.* **11**, 761-767.
38. George, A.R., and Howlett, D.R. (1999) *Biopolymers* **50**, 733-741.
39. Yamada, N., Ariga, K., Naito, M., Matsubara, K., and Koyama, E. (1998) *J. Am. Chem. Soc.* **120**, 12192-12199.
40. Hilbich, C., Kisterswoike, B., Reed, J., Masters, C.L., and Beyreuther, K. (1992) *J. Mol. Biol.* **228**, 460-473.
41. Wood, S.J., Wetzel, R., Martin, J.D., and Hurle, M.R. (1995) *Biochemistry* **34**, 724-730.
42. Fay, D.S., Fluet, A., Johnson, C.J., and Link, C.D. (1998) *J. Neurochem.* **71**, 1616-1625.
43. Tjernberg, L.O., Naslund, J., Lindqvist, F., Johansson, J., Karlstrom, A.R., Thyberg, J., Terenius, L., and Nordstedt, C. (1996) *J. Biol. Chem.* **271**, 8545-8548.
44. Soto, C., Kindy, M.S., Baumann, M., and Frangione, B. (1996) *Biochem. Biophys. Res. Comm.* **226**, 672-680.
45. Tjernberg, L.O., Lilliehook, C., Callaway, D.J.E., Naslund, J., Hahne, S., Thyberg, J., Terenius, L., and Nordstedt, C. (1997) *J. Biol. Chem.* **272**, 12601-12605.
46. Findeis, M.A., Musso, G.M., Arico-Muendel, C.C., Benjamin, H.W., Hundal, A.M., Lee, J.J., Chin, J., Kelley, M., Wakefield, J., Hayward, N.J., and Molineaux, S.M. (1999) *Biochemistry* **38**, 6791-6800.
47. Weliky, D.P., and Tycko, R. (1996) *J. Am. Chem. Soc.* **118**, 8487-8488.
48. Tycko, R., Weliky, D.P., and Berger, A.E. (1996) *J. Chem. Phys.* **105**, 7915-7930.
49. Tycko, R., and Berger, A.E. (1999) *J. Magn. Reson.* **141**, 141-147.
50. Bennett, A.E., Weliky, D.P., and Tycko, R. (1998) *J. Am. Chem. Soc.* **120**, 4897-4898.

51. Gullion, T., and Schaefer, J. (1989) *J. Magn. Reson.* **81**, 196-200.
52. Pan, Y., Gullion, T., and Schaefer, J. (1990) *J. Magn. Reson.* **90**, 330-340.
53. Anderson, R.C., Gullion, T., Joers, J.M., Shapiro, M., Villhauer, E.B., and Weber, H.P. (1995) *J. Am. Chem. Soc.* **117**, 10546-10550.
54. Bennett, A.E., Rienstra, C.M., Auger, M., Lakshmi, K.V., and Griffin, R.G. (1995) *J. Chem. Phys.* **103**, 6951-6958.
55. Gullion, T., and Vega, S. (1992) *Chem. Phys. Lett.* **194**, 423-428.
56. Bennett, A.E., Ok, J.H., Griffin, R.G., and Vega, S. (1992) *J. Chem. Phys.* **96**, 8624-8627.
57. Hediger, S., Meier, B.H., and Ernst, R.R. (1995) *Chem. Phys. Lett.* **240**, 449-456.
58. Hartzell, C.J., Whitfield, M., Oas, T.G., and Drobny, G.P. (1987) *J. Am. Chem. Soc.* **109**, 5966-5969.
59. Oas, T.G., Hartzell, C.J., McMahon, T.J., Drobny, G.P., and Dahlquist, F.W. (1987) *J. Am. Chem. Soc.* **109**, 5956-5962.
60. Teng, Q., Iqbal, M., and Cross, T.A. (1992) *J. Am. Chem. Soc.* **114**, 5312-5321.
61. Bower, P.V., Oyler, N., Mehta, M.A., Long, J.R., Stayton, P.S., and Drobny, G.P. (1999) *J. Am. Chem. Soc.* **121**, 8373-8375.
62. Herzfeld, J., and Berger, A.E. (1980) *J. Chem. Phys.* **73**, 6021.
63. Wolman, M., and Bubis, J.J. (1965) *Histochemie* **4**, 351-356.
64. Blake, C., and Serpell, L. (1996) *Structure* **4**, 989-998.
65. Wishart, D.S., Sykes, B.D., and Richards, F.M. (1991) *J. Mol. Biol.* **222**, 311-333.
66. Long, H.W., and Tycko, R. (1998) *J. Am. Chem. Soc.* **120**, 7039-7048.
67. Weliky, D.P., Bennett, A.E., Zvi, A., Anglister, J., Steinbach, P.J., and Tycko, R. (1999) *Nat. Struct. Biol.* **6**, 141-145.
68. Bennett, A.E., Rienstra, C.M., Griffiths, J.M., Zhen, W.G., Lansbury, P.T., and Griffin, R.G. (1998) *J. Chem. Phys.* **108**, 9463-9479.
69. Wishart, D.S., Bigam, C.G., Holm, A., Hodges, R.S., and Sykes, B.D. (1995) *J. Biomolec. NMR* **5**, 67-81.
70. Spera, S., and Bax, A. (1991) *J. Am. Chem. Soc.* **113**, 5490-5492.
71. Straus, S.K., Bremi, T., and Ernst, R.R. (1997) *J. Biomolec. NMR* **10**, 119-128.
72. Straus, S.K., Bremi, T., and Ernst, R.R. (1998) *J. Biomolec. NMR* **12**, 39-50.
73. Hong, M. (1999) *J. Biomolec. NMR* **15**, 1-14.
74. Hong, M., and Jakes, K. (1999) *J. Biomolec. NMR* **14**, 71-74.
75. McDermott, A., Polenova, T., Bockmann, A., Zilm, K.W., Paulsen, E.K., Martin, R.W., and Montelione, G.T. (2000) *J. Biomolec. NMR* **16**, 209-219.
76. Nomura, K., Takegoshi, K., Terao, T., Uchida, K., and Kainosho, M. (1999) *J. Am. Chem. Soc.* **121**, 4064-4065.
77. Pauli, J., van Rossum, B., Forster, H., de Groot, H.J.M., and Oschkinat, H. (2000) *J. Magn. Reson.* **143**, 411-416.
78. Weitekamp, D.P. (1983) in *Advances in Magnetic Resonance* (Waugh, J. S., Ed.) pp 111-274, Academic Press, New York.
79. Gorevic, P.D., Castano, E.M., Sarma, R., and Frangione, B. (1987) *Biochem. Biophys. Res. Comm.* **147**, 854-862.
80. Barrow, C.J., and Zagorski, M.G. (1991) *Science* **253**, 179-182.
81. Shao, H.Y., Jao, S.C., Ma, K., and Zagorski, M.G. (1999) *J. Mol. Biol.* **285**, 755-773.

82. Sticht, H., Bayer, P., Willbold, D., Dames, S., Hilbich, C., Beyreuther, K., Frank, R.W., and Rosch, P. (1995) *Eur. J. Biochem.* **233**, 293-298.

Table 1: ^{13}C chemical shifts in $A\beta_{16-22}$ fibrils, determined from the two-dimensional ^{13}C-^{13}C chemical shift correlation spectrum in Figure 9. Experimental shifts are in ppm, calibrated to an external adamantane standard at 38.56 ppm. Uncertainties due to noise and resonance overlap are approximately ±0.2 ppm. Shifts in parentheses are random coil values from Wishart *et al*. (*69*).

^{13}C site	Leu17	Val18	Phe19, Phe20 (unresolved)	Ala21
CO	172.8 (177.6)	172.1 (176.3)	170.8 (175.8)	173.3 (177.8)
C_α	52.5 (55.1)	59.6 (62.2)	54.5 (57.7)	48.9 (52.5)
C_β	45.2 (42.4)	34.1 (32.9)	42.1 (39.6)	21.9 (19.1)
C_γ	26.9 (26.9)	19.6 (21.1,20.3)	137.5 (138.9)	
C_δ	22.9 (24.9,23.3)		129.5 (131.9)	

Figure Legends

Figure 1: (a) Transmission electron micrograph of fibrils formed by the seven-residue peptide $A\beta_{16-22}$, negatively stained with uranyl acetate. (b) X-ray powder diffraction profile of a fibrillized, lyophilized $A\beta_{16-22}$ sample, showing peaks in the scattering intensity at angles corresponding to 4.7 Å and 9.9 Å periodicities characteristic of amyloid fibrils. The same sample was used in REDOR measurements in Fig. 12a.

Figure 2: One-dimensional ^{13}C NMR spectra of a fibrillized $A\beta_{16-22}$ sample in which 20% of the peptide molecules have ^{13}C labels at carbonyl sites of Val18 and Phe19. The same sample was used for measurements in Figs. 4 and 5. (a) Spectrum obtained at a magic-angle spinning (MAS) frequency of 6.0 kHz. Inset shows partial resolution of signals from the two carbonyl labels. (b) Spectrum obtained at a MAS frequency of 2.0 kHz. Spinning sideband lines typical of rigid carbonyl sites are observed from 90 to 250 ppm. Narrow carbonyl lines and sharp spectral features from natural-abundance ^{13}C between 20 and 60 ppm indicate a well ordered molecular conformation in the fibrils.

Figure 3: Radio-frequency (rf) pulse sequences for two-dimensional (2D) MAS exchange measurements (a) and constant-time double-quantum-filtered dipolar recoupling (CTDQFD) measurements (b). CP represents Hartmann-Hahn cross polarization. x, y, and –x indicate the phases of 90° pulses. τ_e is the exchange period. In 2D MAS exchange measurements, four complete 2D data sets are acquired, with η = x or y, and with rf pulses synchronized with MAS so that either τ_e or $t_1 + \tau_e$ is a multiple of the rotor period τ_R. In CTDQFD measurements, rf-driven recoupling (RFDR) sequences are applied in the three shaded intervals. The double-quantum preparation time is $L\tau_R$. The effective dipolar evolution time is $(M - N)\tau_R$. Double-quantum filtering is accomplished by acquiring signals with overall rf phase shifts $\Delta\phi$ = 0°, 90°, 180°, and 270° and alternately adding and subtracting the signals.

Figure 4: 2D MAS exchange spectrum of the doubly ^{13}C-labeled $A\beta_{16-22}$ sample in Fig. 2, obtained at an MAS frequency of 2.5 kHz and with τ_e = 500 ms. The carbonyl region is shown. Crosspeaks connecting spinning sidebands of the labeled carbonyl sites are observed. The crosspeak amplitudes are analyzed by comparison with numerical simulations to provide constraints on the peptide backbone dihedral angles ϕ and ψ at Phe19, as shown in Fig. 6.

Figure 5: (a) CTDQFD data for the doubly ^{13}C-labeled $A\beta_{16-22}$ sample in Fig. 2, obtained at an MAS frequency of 4.0 kHz, a double-quantum preparation time $L\tau_R$ = 8 ms, and the indicated values of the effective dipolar evolution time $\tau_D = (M - N)\tau_R$. (b) Comparison of experimental signal amplitudes (open circles) with simulated CTDQFD curves assuming ϕ,ψ values for Phe19 of -130°,120° (solid line), –50,-110° (dotted line), and -60°,-40° (dashed line). These ϕ,ψ values correspond roughly to the global and local minima in χ^2 in Fig. 6a and to typical α-helical values and are chosen to illustrate the sensitivity of CTDQFD curves to peptide conformation. Experimental signal amplitudes are in arbitrary units. Error bars indicate the RMS noise in the experimental spectra. Simulated signal amplitudes are scaled for optimal agreement with experimental data as described in the text.

Figure 6: Quantitative analysis of 2D MAS exchange and CTDQFD data in Figs. 4 and 5. Contour plots represent the χ^2 deviation between numerical simulations and experimental data as a function of the ϕ,ψ angles of Phe19 assumed in the simulations. Plots are shown for 2D MAS exchange data alone (a), CTDQFD data alone (b), and the combined data sets (c). The minimum χ^2 value in part c occurs at ϕ,ψ = -130°,115°, indicating a β-strand conformation for $A\beta_{16\text{-}22}$ at the central Phe19 residue in the amyloid fibrils. Lowest contour levels (darkest regions) are at χ^2 = 9, 2, and 12 in (a), (b), and (c), respectively. Higher contours represent increments of one unit in (a) and (b), and two units in (c).

Figure 7: Two-dimensional ^{13}C-^{13}C chemical shift correlation spectrum of a fibrillized $A\beta_{16\text{-}22}$ sample in which the hydrophobic segment from Leu17 through Ala21 is uniformly ^{13}C- and ^{15}N-labeled in 10% of the molecules. The remaining 90% are unlabeled. This spectrum was acquired at a MAS frequency of 24 kHz using a 2D exchange pulse sequence with an exchange period of 2.6 ms for selective observation of crosspeaks between directly-bonded carbon sites. The 2D assignments of carbonyl, C_α, C_β, C_γ, and C_δ signals for Leu17, Val18, Phe19 and Phe20, and Ala21 in $A\beta_{16\text{-}22}$ are indicated by the arrows. Signals from the two phenylalanines are not resolved from one another. The assignments are summarized in Table 1.

Figure 8: (a) Rf pulse sequence for ^{13}C multiple quantum (MQ) NMR measurements. MQ excitation sequences are applied during the preparation and mixing periods with durations τ_{MQ} and phase shifts $\Delta\phi$. τ is a delay for dephasing of ^{13}C coherences. MQ signals of different order are separated by incrementation of the preparation period phase according to $\phi_k = 2\pi k / 32$, with k = 0, 1, 2, ... , 31 and Fourier transformation of the ^{13}C NMR signals with respect to k and t_2. (b) Pulse cycle applied during the preparation and mixing periods. Solid bars represent 180° inserted between the 90° pulses to remove chemical shifts. The pulse cycle is repeated n_c times, making $\tau_{MQ} = n_c\tau_c$. 45° pulses with phases y and –y are applied at the beginning and end of the preparation and mixing periods, producing effective dipole-dipole couplings that are time-reversible by a phase shift $\Delta\phi = \pi$.

Figure 9: Experimental ^{13}C MQNMR spectra of a fibrillized $A\beta_{16\text{-}22}$ sample with ^{13}C labels at the methyl carbon of Ala21. The amplitudes of 2- and 3-quantum signals increase relative to the 1-quantum amplitude with increasing τ_{MQ}, but no higher-order MQ signals are detected. Vertical scales are adjusted for each τ_{MQ} so that the 1-quantum peak is clipped at 25% of its full height.

Figure 10: Schematic representations of hypothetical in-register, parallel (a) and in-register, antiparallel (b) β-sheet organizations in $A\beta_{16\text{-}22}$ fibrils. Dotted lines indicate hydrogen bonds. Black dots indicate the locations of Ala21 methyl carbons that are labeled in MQNMR measurements.

Figure 11: Comparison of experimental MQ signal amplitudes (solid bars) with simulations for hypothetical in-register, antiparallel (bars filled with slanted lines) and in-register, parallel (cross-hatched bars) organizations of β-sheets, as in Fig. 10. MQ amplitudes are presented on a logarithmic scale because they vary over more than two orders of magnitude. Parallel β-sheet simulations greatly overestimate the amplitudes of 3- and 4-quantum signals relative to the 2-

quantum amplitude. Antiparallel β-sheet simulations are in better agreement with experiments. Experimental MQ amplitudes are normalized to a 1-quantum amplitude of 100. Simulated MQ amplitudes are scaled for optimal agreement with experiments at each τ_{MQ} value as described in the text. Uncertainty in the experimental amplitudes due to the RMS noise in the experimental spectra is approximately ±0.16.

Figure 12: (a) ^{13}C-detected $^{13}C/^{15}N$ REDOR measurements on fibrillized $A\beta_{16-22}$ samples with ^{13}C labels at the carbonyl carbon of Leu17 and ^{15}N labels at the amide nitrogen of Ala21 (LA sample, filled circles) or Phe20 (LF sample, filled triangles). The dependence of the normalized REDOR difference signal $\Delta S/S_0$ on the dephasing time τ_{REDOR} is determined by ^{13}C-^{15}N distances and directions. Experimental data are determined from integrals of carbonyl signals in REDOR spectra. Error bars are determined solely from the RMS noise in the experimental spectra. (b) Antiparallel β-sheet geometry assumed in REDOR simulations. Filled circle, thick-walled circles, and thin-walled circles represent a ^{13}C label at the Leu17 carbonyl, ^{15}N labels at the two nearest Ala21 amides, and ^{15}N labels at the two nearest Phe20 amides. Simulated REDOR curves in part a assume an idealized in-register, antiparallel structure with hydrogen-bonding between Leu17 and Ala21 (d_1 = 4.2 Å, d_2 = 9.4 Å, d_3 = 3.4 Å, $\theta_1 = 0°$, $\theta_2 = 90°$, solid line for LA sample, dashed line for LF sample) or a modified geometry that leads to an improved fit to the experimental data (d_1 = 4.4 Å, d_2 = 10.0 Å, d_3 = 3.4 Å, $\theta_1 = 10°$, $\theta_2 = 78°$, closely-spaced dotted line for LA sample, widely-spaced dotted line for LF sample).

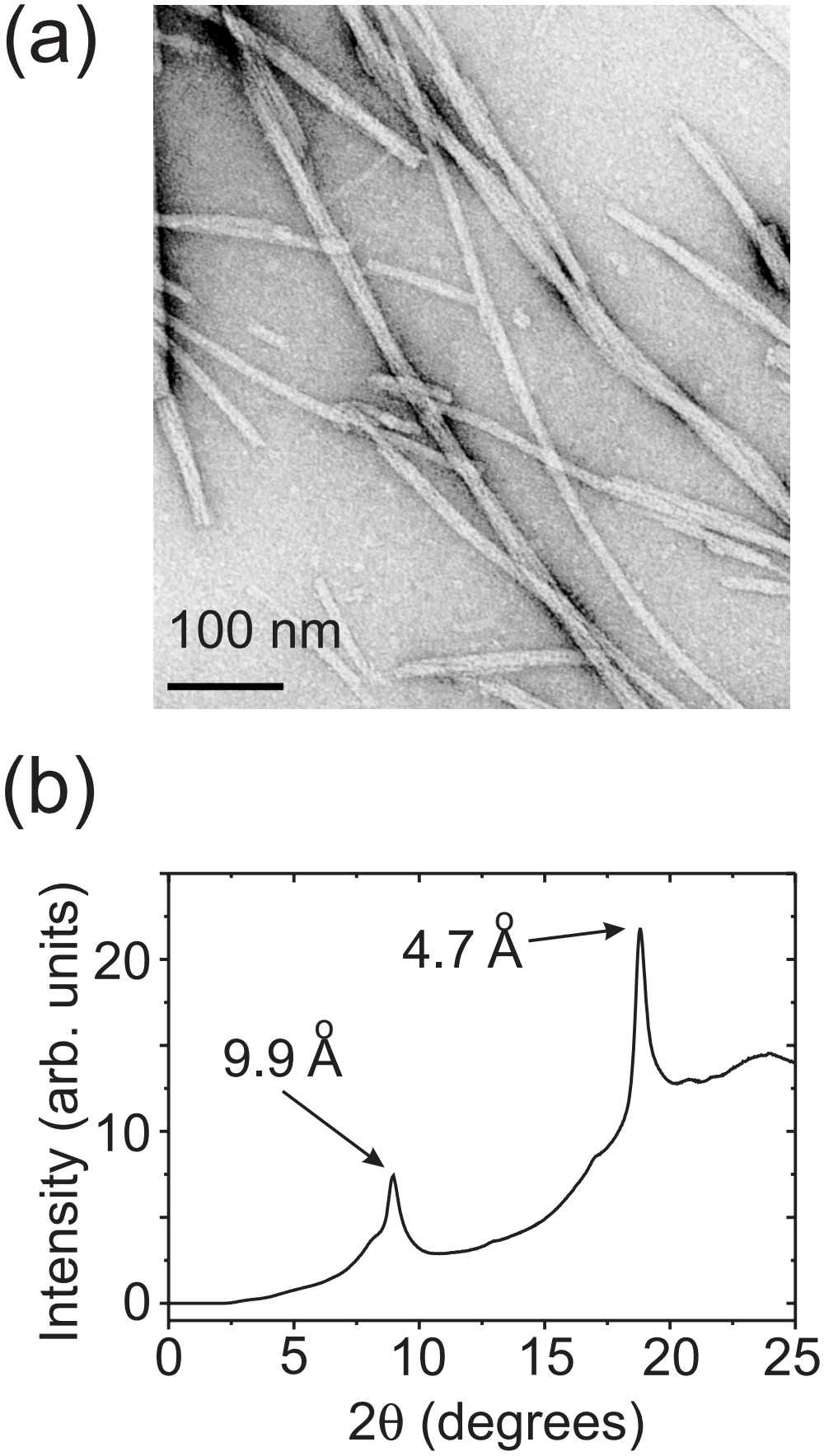

Figure 1, Balbach et al., "Amyloid Fibril Formation ... "

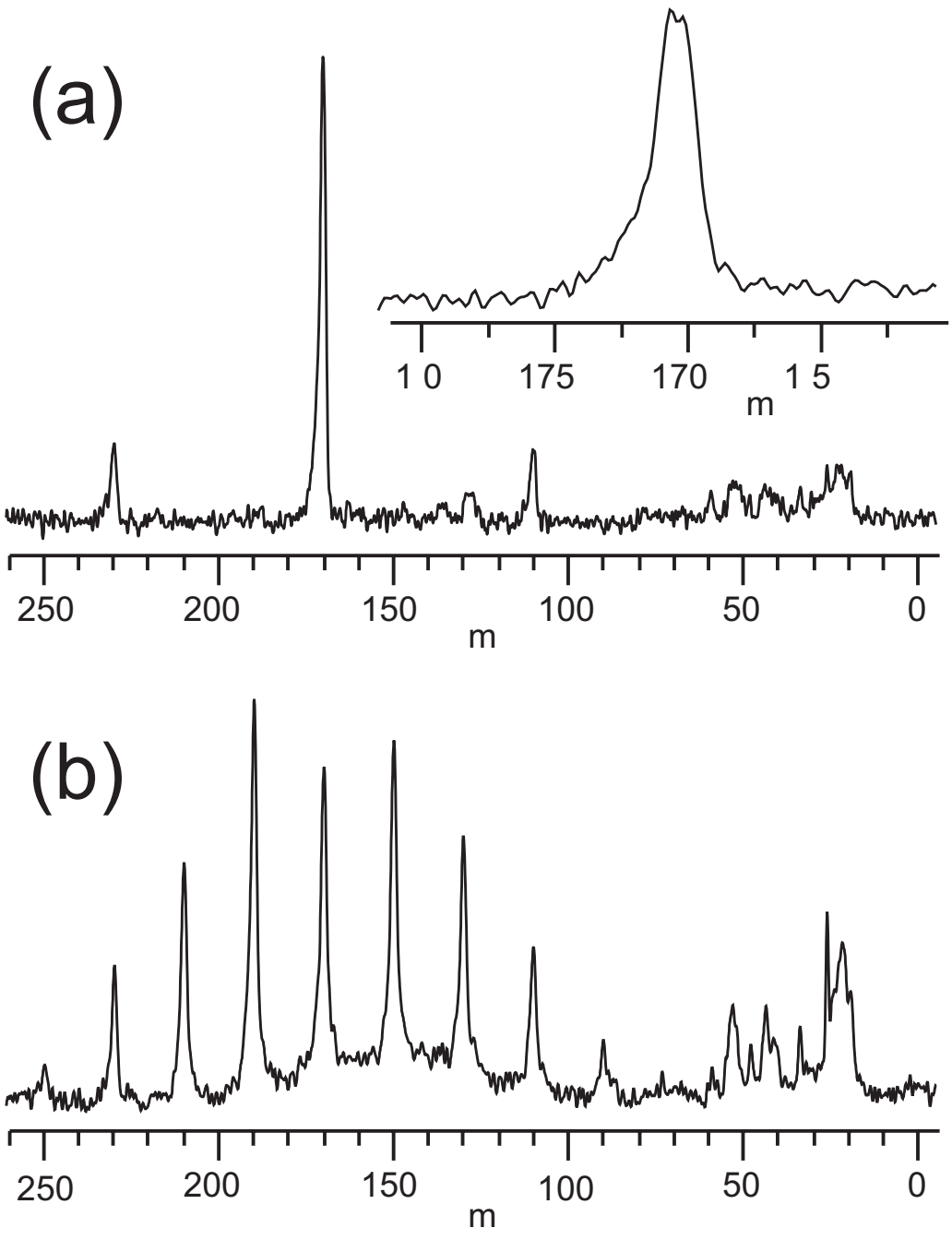

Figure 2, Balbach et al., "Amyloid Fibril Formation ... "

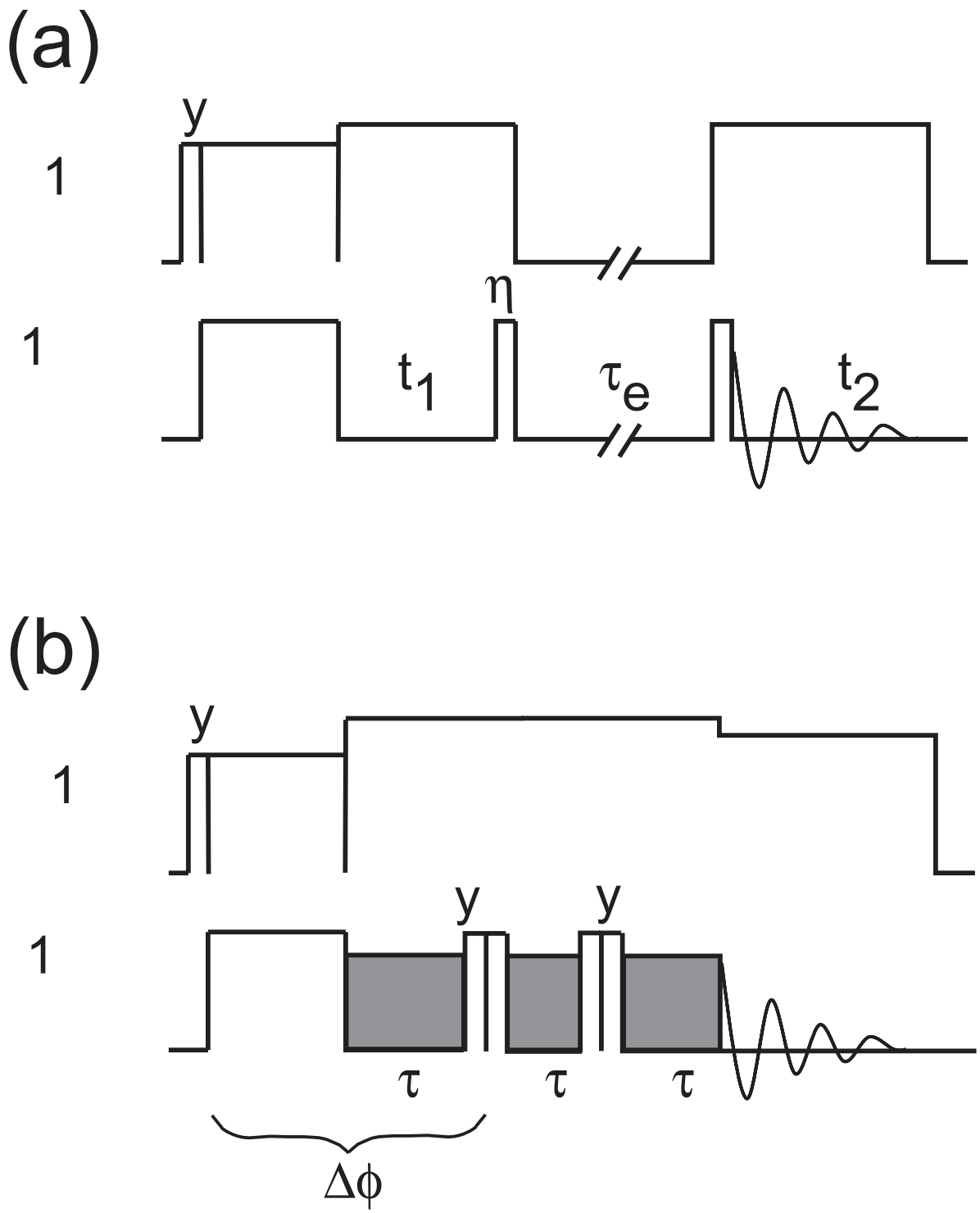

Figure , Balbach et al., "Amyloid Fibril Formation ... "

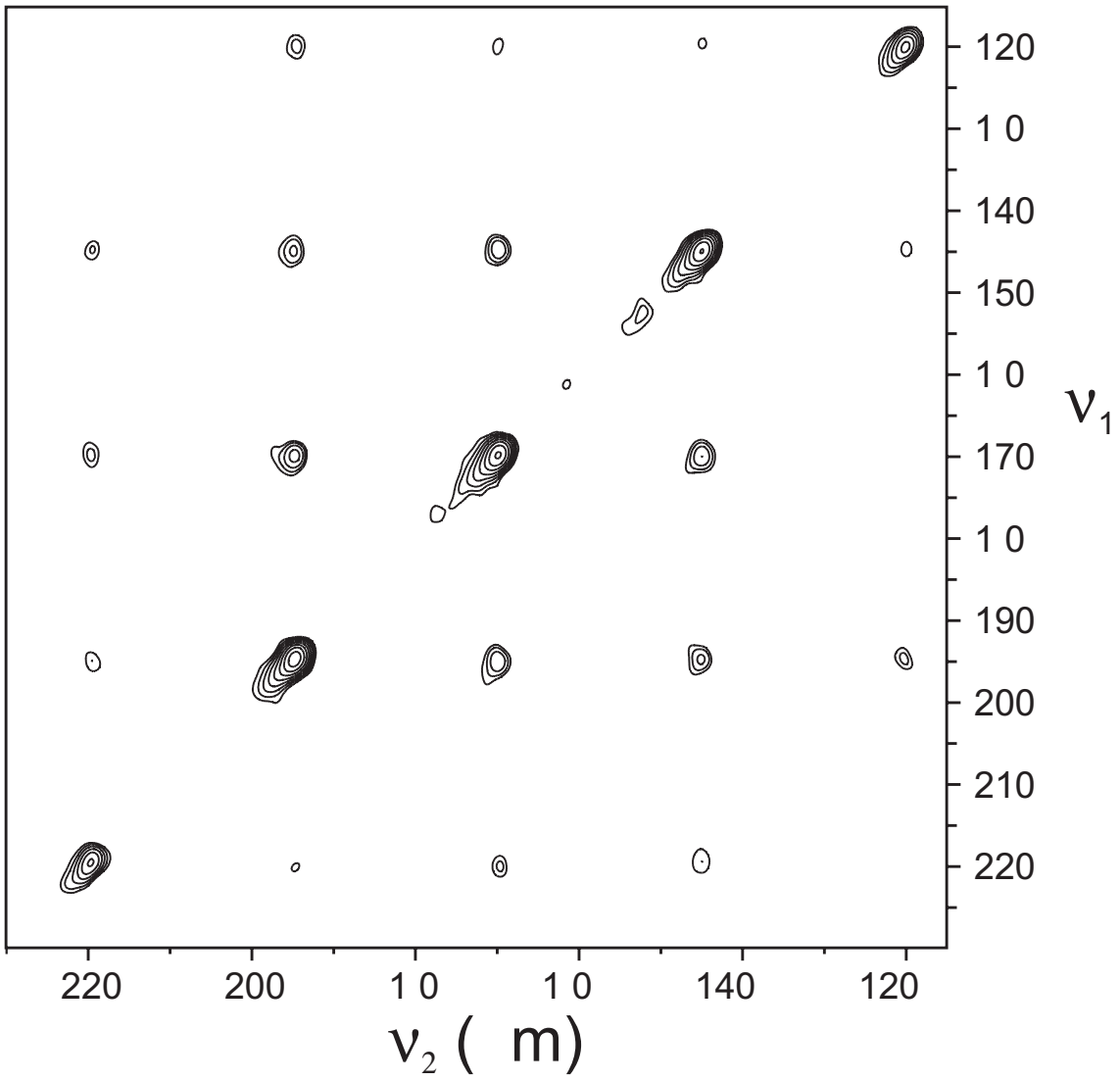

Figure 4, Balbach et al., "Amyloid Fibril Formation ... "

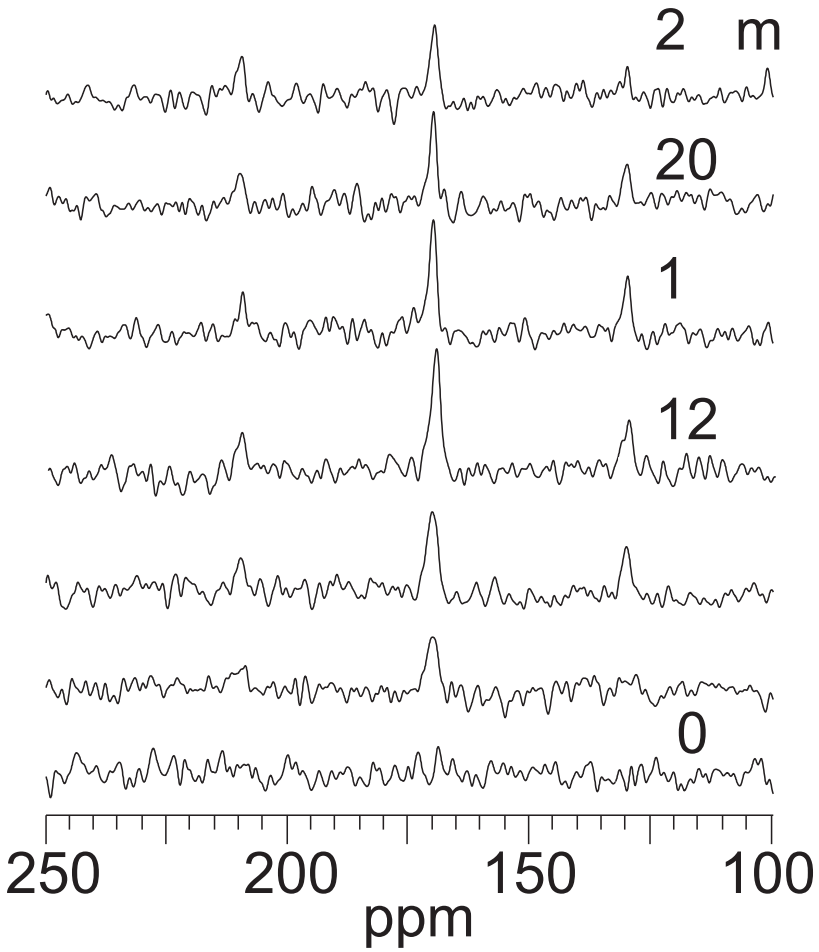

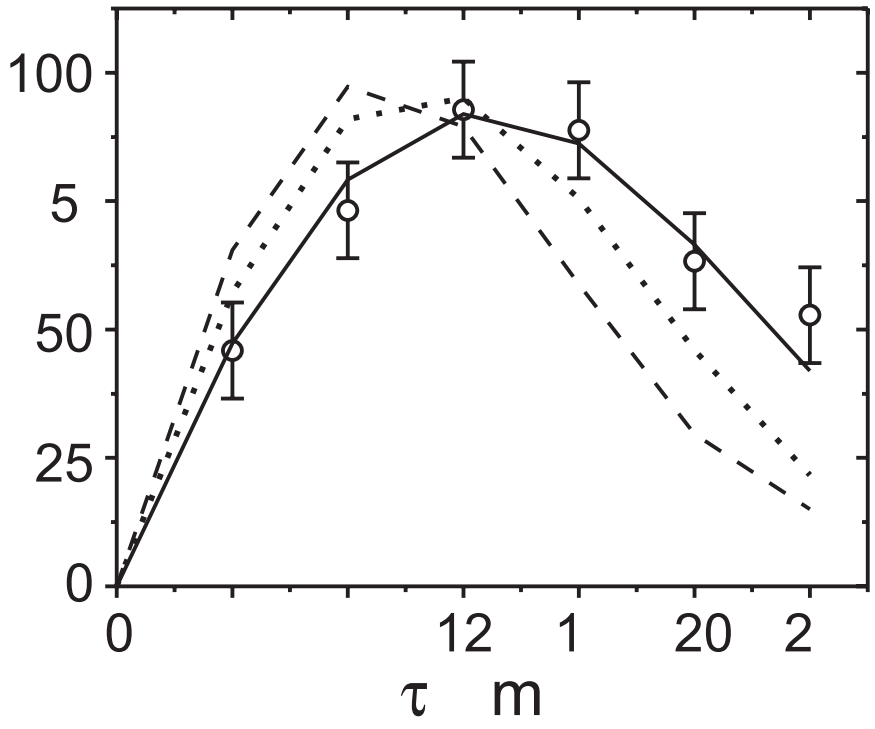

5 m m

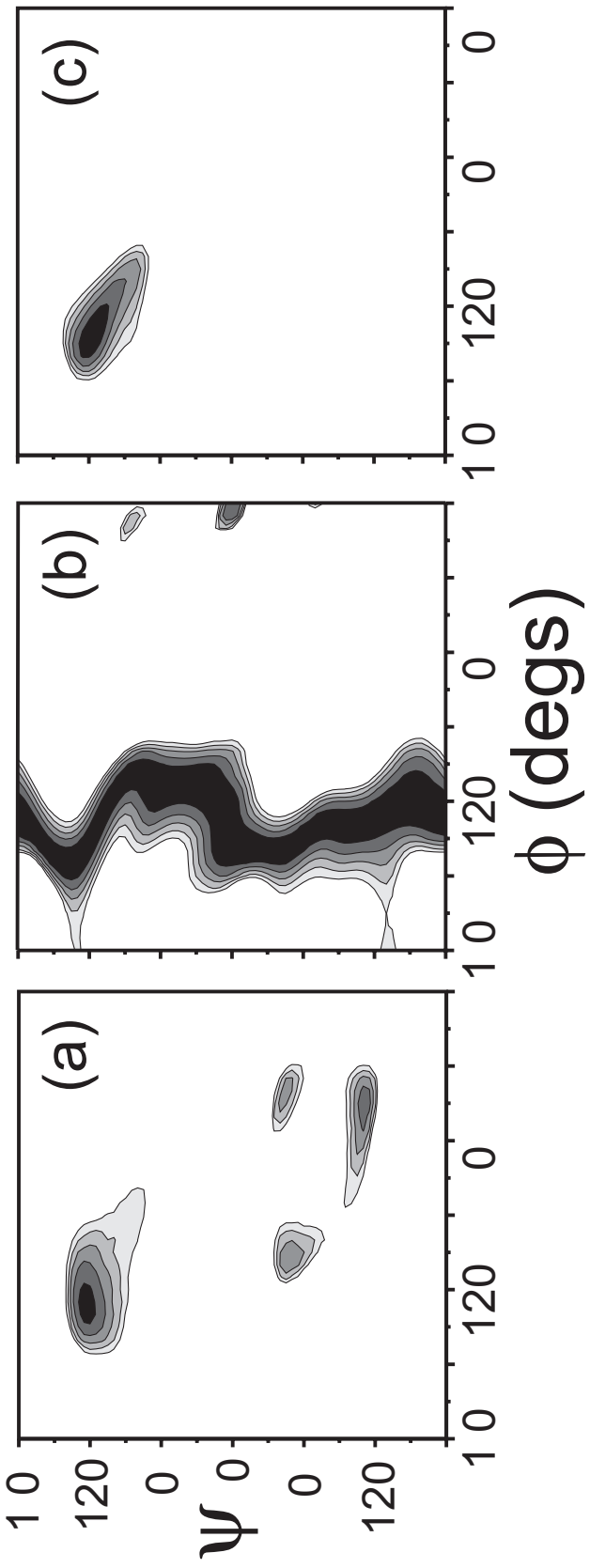

Figure , Balbach et al., "Amyloid Fibril Formation ... "

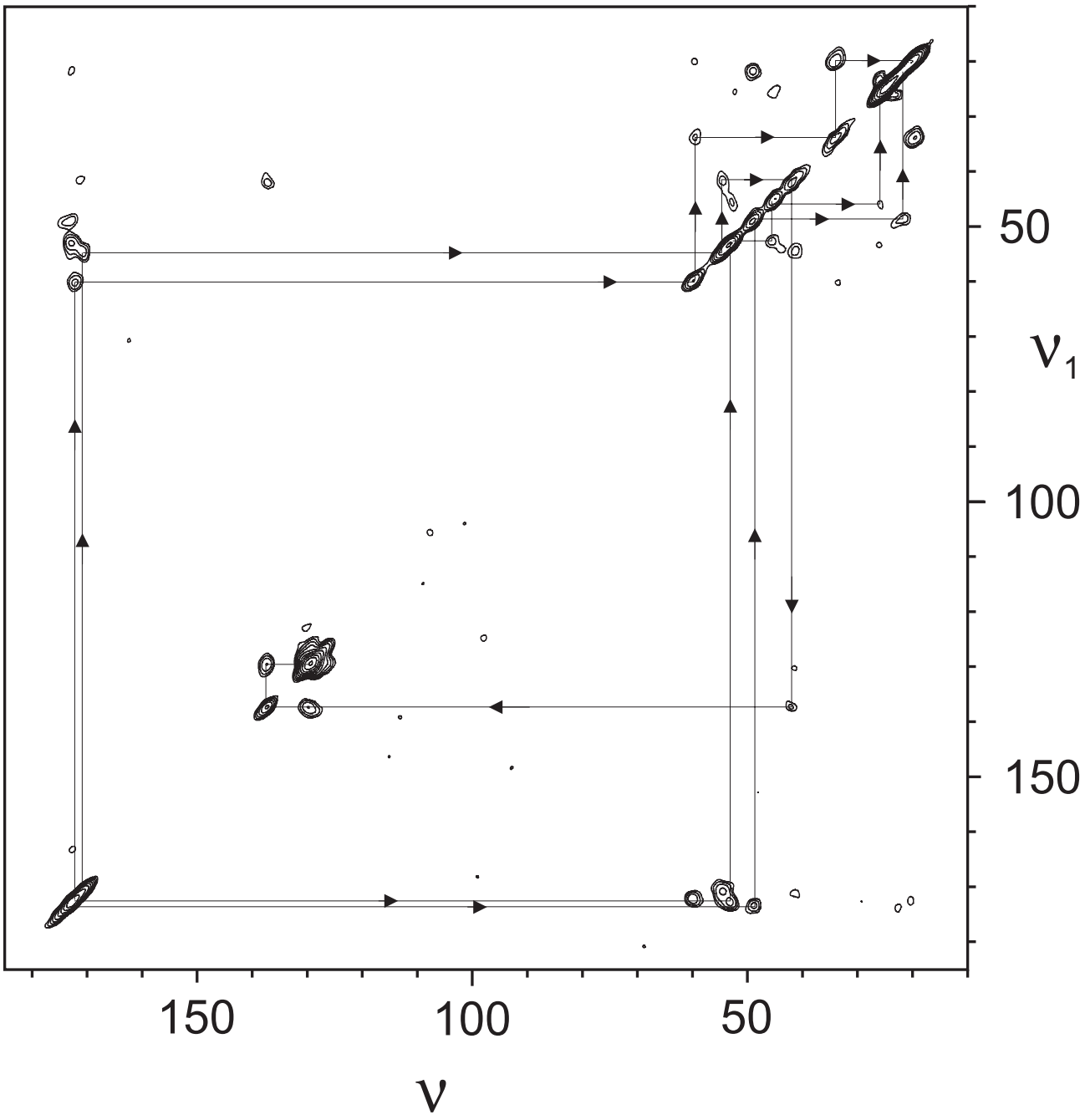
50
100
150
ν_1
150
100
50
ν

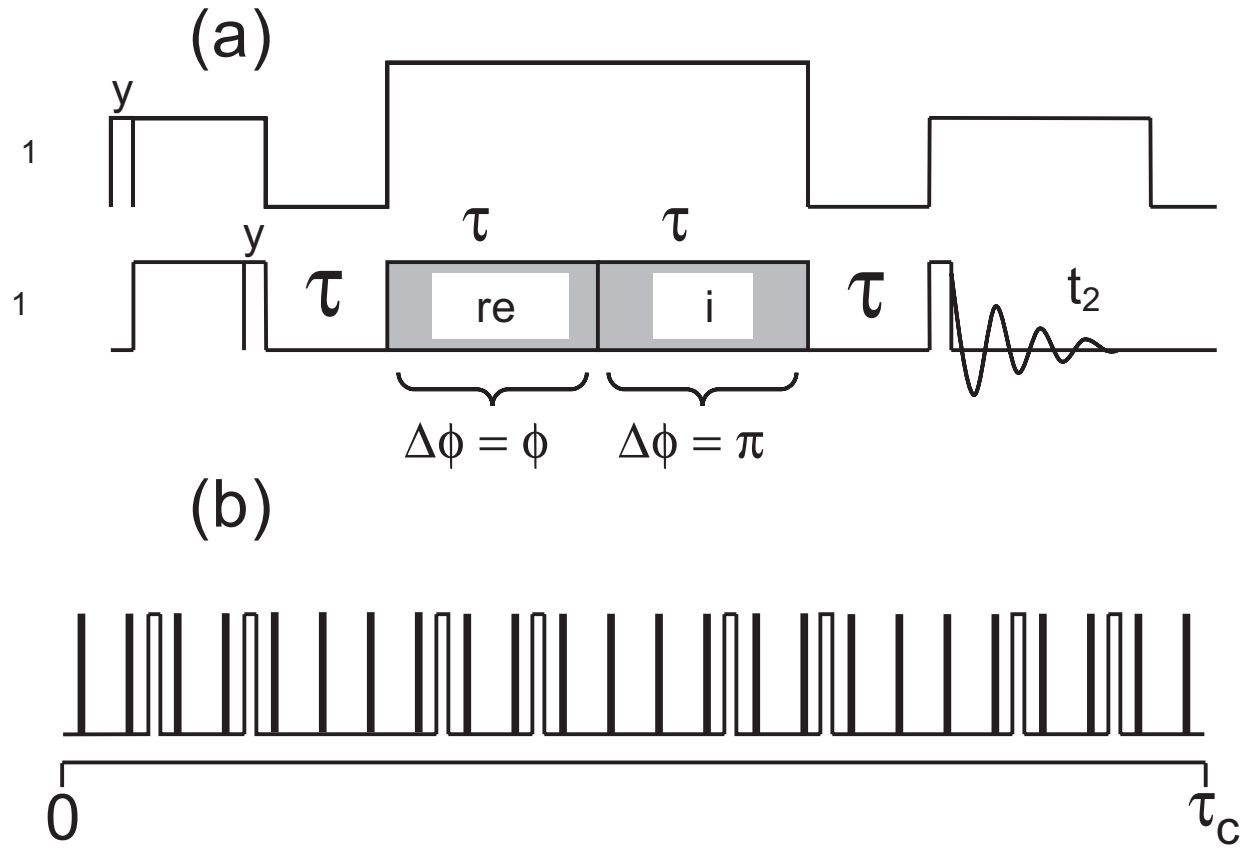

Figure , Balbach et al., "Amyloid Fibril Formation ... "

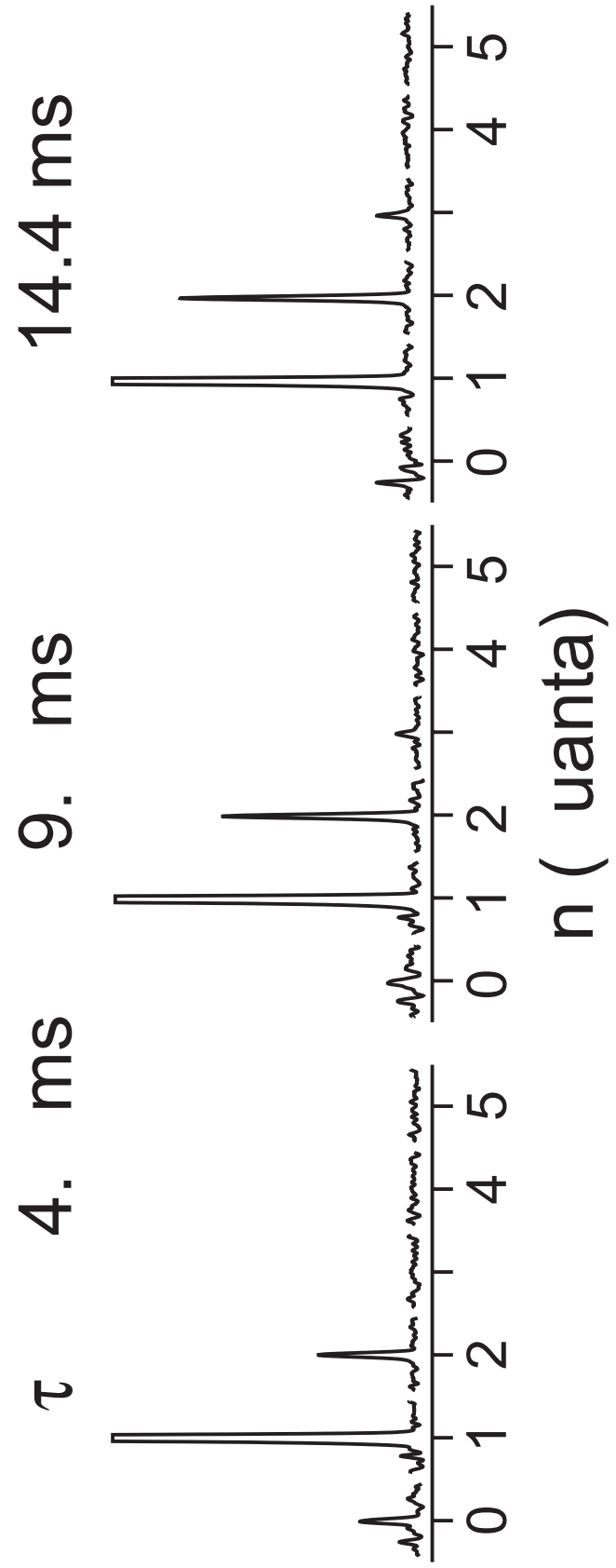

Figure 9, Balbach et al., "Amyloid Fibril Formation ... "

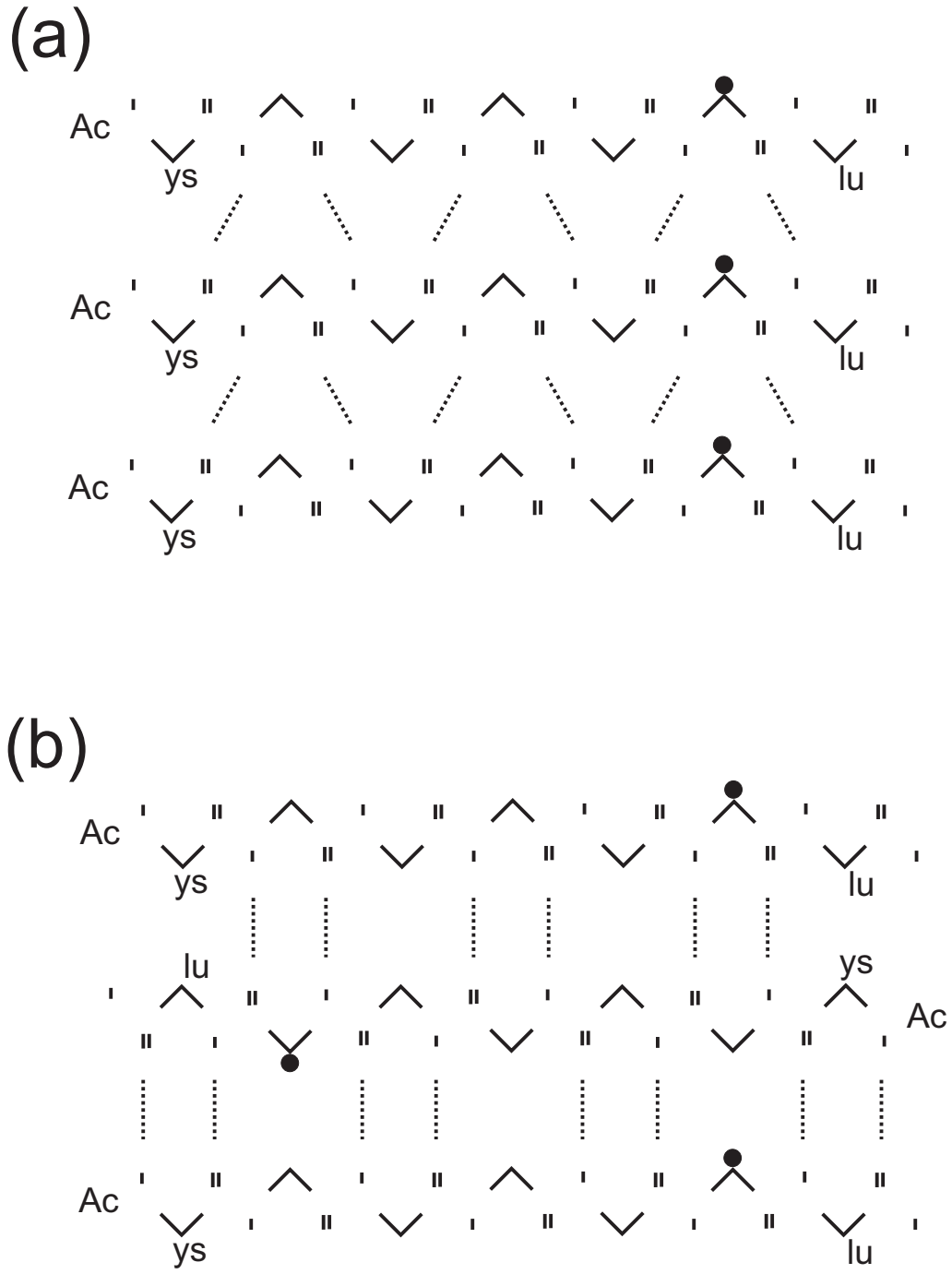

Figure 10, Balbach et al., "Amyloid Fibril Formation ... "

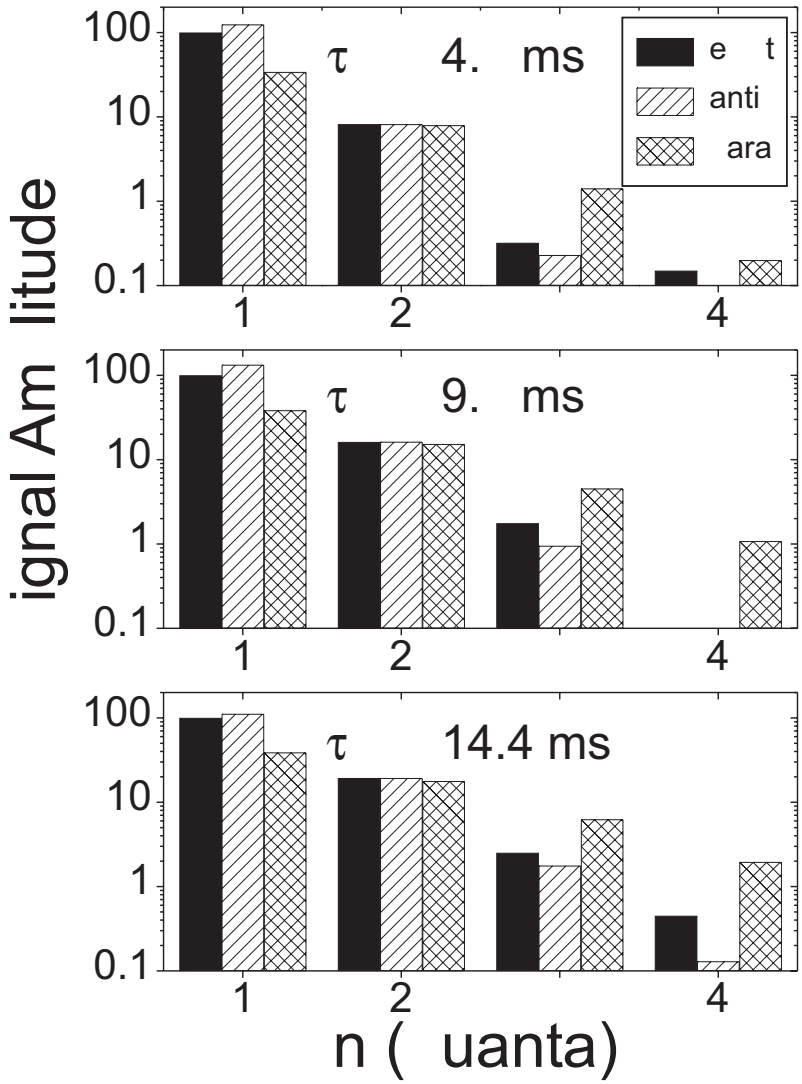

Figure 11, Balbach et al., "Amyloid Fibril Formation ... "

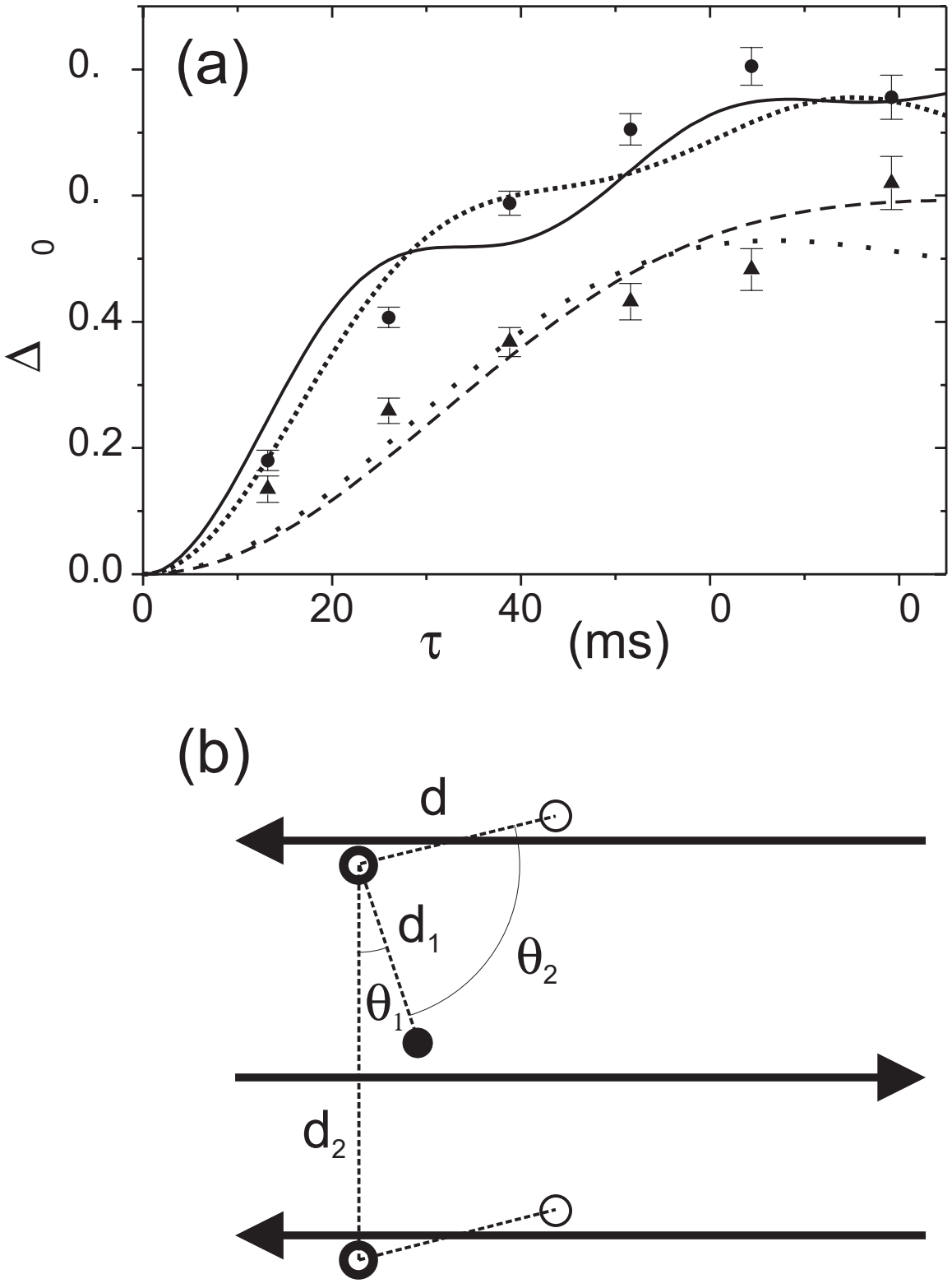

Figure 12, Balbach et al., "Amyloid Fibril Formation ... "